Global climate simulations at 3,000-year intervals for the last 21,000 years with the GENMOM coupled atmosphere-ocean model

J. R. Alder and S. W. Hostetler

Jay R. Alder, US Geological Survey, College of Earth, Ocean and Atmospheric Sciences, Oregon State University, Corvallis, Oregon 97331, United States, jalder@usgs.gov

Steven W. Hostetler, US Geological Survey, College of Earth, Ocean and Atmospheric Sciences, Oregon State University, Corvallis, Oregon 97331, United States, swhostet@usgs.gov

Corresponding author address: Jay Alder
E-mail: jalder@usgs.gov

Abstract

We apply GENMOM, a coupled atmosphere-ocean climate model, to simulate eight equilibrium time slices at 3000-yr intervals for the past 21,000 years forced by changes in Earth-Sun geometry, atmospheric greenhouse gases (GHGs), continental ice sheets and sea level. Simulated global cooling during the Last Glacial Maximum (LGM) is 3.8 °C and the rate of post-glacial warming is in overall agreement with recently published temperature reconstructions. The greatest rate of warming occurs between 15 and 12 ka (2.4 °C over land, 0.7 °C over oceans and 1.4 °C globally) in response to changes in radiative forcing from the diminished extent of the Northern Hemisphere (NH) ice sheets and increases in GHGs and NH summer insolation. The modeled LGM and 6 ka temperature and precipitation climatologies are generally consistent with proxy reconstructions, the PMIP2 and PMIP3 simulations, and other paleoclimate data-model analyses. The model does not capture the mid-Holocene 'thermal maximum' and gradual cooling to pre-industrial global temperature found in the data. Simulated monsoonal precipitation in North Africa peaks between 12 and 9 ka at values ~50% greater than those of the PI, and Indian monsoonal precipitation peaks at 12 and 9 ka at values ~45% greater than the PI. GENMOM captures the reconstructed LGM extent of NH and Southern Hemisphere (SH) sea ice. The simulated present-day Antarctica Circumpolar Current (ACC) is ~48% weaker than the observed (62 versus 119 Sv). The simulated present-day Atlantic Meridional Overturning Circulation (AMOC) of 19.3 ± 1.4 Sv on the Bermuda Rise (33°N) is comparable with observed value of 18.7 ± 4.8 Sv. AMOC at 33°N is reduced by ~15% during the LGM, and the largest post-glacial increase (~11%) occurs during the 15 ka time slice.

1 Introduction

The history of the climate system over the past 21,000 years reflects the combined changes in earth-sun orbital geometry, atmospheric greenhouse gas concentrations (GHG), the extent of the Northern Hemisphere (NH) ice sheets, and sea level. GHG levels were lowest during the Last Glacial Maximum (LGM, ~21,000 years ago, 21 ka) and increased thereafter to pre-industrial (PI) levels (Brook et al., 2000; Monnin et al., 2001; Sowers et al., 2003). The LGM is further characterized by the large Laurentide (LIS), Cordilleran (CIS) and Fennoscandian (FIS) ice sheets. The height and extent of the ice sheets altered atmospheric circulation patterns, and the extent increased the NH albedo thereby altering the global radiative balance. The effect of the ice sheets on climate progressively diminished from the LGM to the early Holocene as global warming driven by increasing GHGs combined with changes in NH summer insolation to accelerate ice sheet ablation. Abrupt departures from the comparatively smooth transition from the LGM through the Holocene, such as Heinrich and Dansgaard-Oeschger events, the Bølling-Allerød (BA), and the Younger Dryas (YD), are evident in geologic records, and these events likely influenced the overall trajectory of the deglaciation.

The climate of the past 21,000 years has been studied extensively, beginning with three international collaborative projects: the Long range Investigation, Mapping, and Prediction (CLIMAP; CLIMAP Project Members, 1981) and the Cooperative Holocene Mapping Project (COHMAP; COHMAP Members, 1988), which evolved into the Testing Earth System Models with Paleoenvironmental Observations (TEMPO) project (Kutzbach et al., 1996a; 1998). CLIMAP focused on reconstructing the LGM climate, COHMAP focused on reconstructing the climate of seven time periods (18, 15, 12, 9, 6, 3

ka), and TEMPO focused on reconstructing the climate of 21, 16, 14, 11 and 6 ka. These three projects pioneered data-model comparison through integrating climate model simulations and paleoclimatic data, which motivated the development of new techniques for analyzing geologic data and led to improvements in general circulation models.

More recently, the Palaeoclimate Modelling Intercomparison Project (PMIP) is actively working to advance reconstruction of LGM and 6 ka climate through model-to-model evaluations and data-model comparisons. PMIP has now entered the third phase (PMIP3; Braconnot et al., 2012) and is a component of phase 5 of the Climate Model Intercomparison Project (CMIP5). In contrast to CLIMAP, COHMAP, TEMPO and earlier PMIP model experiments that employed fixed sea surface temperatures (SST) and mixed-layer ocean models, some of the PMIP2 experiments and all of the PMIP3 experiments include fully coupled ocean and atmospheric models. Braconnot et al. (2012) review some of the highlights of the PMIP2 experiments and the design of the PMIP3 experiments and Harrison et al. (2013) evaluate the PMIP3 and PMIP2 simulations of LGM and 6 ka climates with data-model comparisons. In addition, continuous simulations of climate over the last 21 ka have been achieved with earth system models of intermediate complexity (e.g., Timm and Timmermann, 2007), and the TraCE-21ka project at the National Center for Atmospheric Research (NCAR) conducted continuous, transient climate simulations from 22 ka to 6.5 ka with the coupled NCAR Community Climate System Model (Liu et al., 2009). Singarayer and Valdes (2010) simulated the climate of the last 120,000 years using model snapshots at 4 ka and 1 ka intervals.

Here we explore past changes in late-Pleistocene climate using the coupled Atmosphere-Ocean General Circulation Model (AOGCM) GENMOM. We simulated

multi-century time slices that span the interval from LGM to pre-industrial (PI) every three thousand years (21, 18, 15, 12, 9, 6, 3 ka and PI). The simulations were run with prescribed insolation, GHG concentrations, continental ice sheets, land extent and sea level as boundary conditions. We analyze the within and between climatology of the time slices and compare the 21 ka and 6 ka results with terrestrial and marine climate reconstructions and results from the PMIP2 and PMIP3 simulations. The goal of our simulations is to adopt a methodological framework similar to that of PMIP to simulate time slices between the LGM and mid-Holocene. The simulations also serve as a base line for applying GENMOM to more detailed and focused studies of late-Pleistocene climate such as quantifying the effects of freshwater forcing and dynamic vegetation feedbacks.

2 Methods

2.1 Model description

GENMOM combines version 3 of the GENESIS atmospheric model (Pollard and Thompson, 1997; Thompson and Pollard, 1995; 1997) with version 2 of the Modular Ocean Model (MOM2, Pacanowski, 1996). Version 3 of GENESIS (Alder et al., 2011; Kump and Pollard, 2008; Pollard and Thompson, 1997; Zhou et al., 2008) incorporates the NCAR CCM3 radiation code (Kiehl et al., 1998). GENESIS has been developed with an emphasis on representing terrestrial physical and biophysical processes, and for application to paleoclimate experiments. Earlier versions of GENESIS (Pollard and Thompson, 1994; 1995; 1997; Thompson and Pollard, 1995; 1997) have been applied in a wide range of modern and paleoclimate studies (Beckmann et al., 2005; Bice et al., 2006; DeConto et al., 2007; 2008; Horton et al., 2007; Hostetler et al., 2006; Miller et al.,

127 2005; Poulsen et al., 2007a; 2007b; Ruddiman et al., 2005; Tabor et al., 2014), and
128 GENESIS simulations with fixed and slab ocean SSTs were included in PMIP1
129 (Joussaume et al., 1999; Pinot et al., 1999; Pollard et al., 1998).

130 In our simulations, we employ a coupled model with T31 spectral truncation,
131 which corresponds to a grid of 96 longitudes (3.75°) by 48 Gaussian latitudes (~3.71°).
132 The atmosphere is represented by 18 vertical sigma levels with mid-layers ranging from
133 0.993 at the surface to 0.005 at the tropopause. GENESIS includes the Land Surface
134 eXchange model, LSX, (Pollard and Thompson, 1995) to simulate surface processes and
135 to account for the exchange of energy, mass and momentum between the land surface and
136 the atmospheric boundary layer. MOM2 has 20 fixed-depth vertical levels and is
137 implemented on essentially the same T31 horizontal grid as GENESIS through cosine-
138 weighted distortion (Pacanowski, 1996). Sea ice is simulated by a three-layer model that
139 accounts for local melting, freezing, and fractional cover (Harvey, 1988; Semtner, 1976)
140 and includes the dynamics associated with wind and ocean current using the cavitating-
141 fluid model of Flato and Hibler (1992). The atmospheric and ocean models interact every
142 six hours without flux corrections.

143 GENMOM reproduces observed global circulation patterns, such as the seasonal
144 change in the position and strength of the jetstreams and the major semi-permanent sea
145 level pressure centers (Alder et al., 2011). The simulated present-day (PD) 2-m air
146 temperature climatology (Table 1) is 0.8 ºC colder than observations globally, 0.7 ºC
147 colder over oceans, and 0.9 ºC colder over land. Similar to other AOGCMs (e.g., Lee and
148 Wang, 2014), GENMOM produces a split ITCZ over the equatorial Pacific Ocean.

149 The pre-industrial Atlantic Meridional Overturning Circulation (AMOC)
150 simulated by GENMOM is 19.3 ± 1.4 Sv, which is stronger than, but comparable to, the
151 observed value of 17.4 Sv (Srokosz et al., 2012). Simulated SSTs display a warm bias in
152 some regions of the Southern Ocean, primarily south of 50ºS around Antarctica, and a
153 warm bias exceeding ~2 ºC between 200–1000 m depth in parts of the tropics and mid-
154 latitudes. Alder et al. (2011) note that the warm bias in the Southern Ocean is associated
155 with the relatively weak Antarctic Circumpolar Current (ACC) in GENMOM (62 Sv
156 versus the observed value of 119 Sv) and Deacon Cell upwelling which allows excessive
157 vertical mixing in the present-day GENMOM simulation, and together reduce sea ice
158 around Antarctica, particularly during summer. Both of these features are present to some
159 extent in our suite of simulations. We tested the Gent-McWilliams vertical ocean mixing
160 scheme (Gent and Mcwilliams, 1990) in GENMOM but it did not improve the Southern
161 Ocean warm bias, so we did not implement it in our paleosimulations.
162 The climate sensitivity of GENMOM for a doubling of CO_2 from present day is
163 2.2 ºC, which is in the lower range of other coupled AOGCMs (Meehl et al., 2007) and is
164 consistent with recent estimates of 2.7 ºC based on the PMIP3 LGM simulations
165 (Harrison et al., 2013) and paleodata-model estimates of 2.8 ºC (Annan and Hargreaves,
166 2013) and 2.3 ºC (Schmittner et al., 2011b).
167 Reflecting lower GHG concentrations, the average NH 2-m temperature in our PI
168 simulation is 0.79 °C cooler than our PD simulation, where as the PD simulation is 1.97
169 ºC cooler than observations and reflects the lower GHG concentrations specified in the PI
170 simulation (Tables 1 and 2). The PI-to-PD warming in the NH is similar to the observed
171 warming of ~0.6 – 0.9 °C (Brohan et al., 2006) and is in the range of response of other

172 climate models (e.g., Otto-Bliesner et al., 2006b). The greatest regional warming between
173 the in the PD simulation (not shown) is ~3 °C over the high northern latitudes and
174 northern polar regions during boreal autumn, winter and spring, consistent with the
175 observed polar amplification (Hassol, 2004).

176 **2.2 Experimental design**

177 We applied GENMOM to eight time periods for 21, 18, 15, 12, 9, 6, 3 ka and pre-
178 industrial. We prescribed insolation at the top of atmosphere for each time slice (Fig. 1)
179 by specifying appropriate orbital parameter values for precession, obliquity and
180 eccentricity (Table 1, Berger and Loutre, 1991). The solar constant was set to 1367 W m^{-2}
181 for all time periods. We estimated GHG concentrations from ice-core records by applying
182 a ±300 yr averaging window centered on the time period of interest (Table 1), and we
183 specified the PMIP3 GHG concentrations for our PI simulation (Braconnot et al., 2007a).

184 To derive continental ice sheets for the time slices, we used the ICE-4G
185 reconstructions (Peltier, 2002) for the Fennoscandian (FIS) and Cordilleran (CIS), and
186 the Oregon State University Laurentide Ice Sheet (OSU-LIS) reconstruction (Hostetler et
187 al., 1999; Licciardi et al., 1998) (Fig. 2). The ICE-6G reconstruction was not available for
188 our 8 time slices at time we began our simulations. However, the OSU-LIS
189 reconstruction has similar ice sheet topography to that of ICE-6G (Ullman et al., 2014)
190 and was available for our simulation periods. The combination of OSU-LIS and ICE-4G
191 enables us to use a more realistic LIS topography than that of ICE-5G, particularly over
192 the LIS during the deglacial, and facilitates adjusting sea level throughout our time slices.
193 A similar ice sheet configuration (OSU-LIS and ICE5-G) was used as a boundary
194 condition in the NASA GISS-E2-R LGM simulation submitted to the PMIP3 archive

(Ullman et al., 2014). We specified the 10 ka OSU-LIS ice sheet to ensure that Hudson Bay remained covered by the LIS at 9 ka (Dyke and Prest, 1987). The ICE-4G reconstruction includes an Eastern Siberian Ice Sheet, which we removed because it did not exist (Felzer, 2001).

Topographic heights of the land masses were altered to reflect relative sea-level change in ICE-4G. We created the topography and land mask for each time slice by applying orographic changes to the present-day Scripps global orography data set (Gates and Nelson, 1975). Orographic changes based on ICE-4G exposed or flooded land grid cells associated with relative sea level (e.g. Indonesia, Papua New Guinea). We set the ocean bathymetry to modern depths for ocean grid cells.

We specified the modern distribution of vegetation (Dorman and Sellers, 1989) for all simulations because reconstructions of global vegetation for all time slices either do not exist or are not well constrained. We note that while setting vegetation to modern distribution for all simulations isolates the period-to-period climate response to other boundary conditions, we do not capture dynamic vegetation-climate feedbacks that may be important in some regions such as North Africa (Kutzbach et al., 1996b; Timm et al., 2010) and the high latitudes of the NH (Claussen, 2009; Renssen et al., 2004). The vegetation type on emergent land cells is set to be the same as neighboring existing land cells. The simulations do not include varying dust forcing across the time slices, which may account for up to 20% of the radiative change (Köhler et al., 2010; Rohling et al., 2012). Freshwater flux from land-based precipitation is globally averaged and spread over the world ocean (Alder et al., 2011).

In accordance with the PMIP3 protocol, to conserve atmospheric mass we compensated for changes in global topography in each time slice by holding global average surface pressure constant. At T31 resolution the Bering Strait and the Strait of Gibraltar are closed in the default MOM2 bathymetry. We conducted sensitivity tests and adjusted the bathymetry to ensure that key passages (e.g. Drake Passage, Norwegian Sea, and Indonesian Throughflow) were adequately represented. Additional sensitivity testing revealed that the modeled AMOC and salinity of the Arctic are very sensitive to the bathymetry of the Norwegian Sea, particularly to the width of the passage between Scandinavia and Greenland as it narrowed by the growth of the FIS. We removed Iceland from the model to ensure that the passage remained sufficiently wide and deep to prevent unrealistic buildup of salinity in the Arctic.

Each time slice simulation was initialized from a cold start (isothermal atmosphere, latitudinally dependent ocean temperature profile, and uniform salinity of 35 ppt) and run for 1,100 years. We exclude the first 1,000 years from our analysis here to allow for spin up of ocean temperatures. The temperature drift in the last 300 years of our simulations (SFig. 1) is acceptably small (Braconnot et al., 2007a; Singarayer and Valdes, 2010) with values of -0.05 ºC/century for the LGM, 0.01 ºC/century for 6 ka, and -0.02 ºC/century for PI. Drift in the LGM and early deglacial simulation is attributed primarily to long-term cooling and the evolution of sea ice in the southern ocean. Simulated AMOC exhibits decadal scale variability, but was free of drift over the last 300 years of the simulations.

In what follows, the monthly averages of the model output are based on the modern calendar as opposed to the angular calendar that changes with Earth-sun

geometry (Pollard and Reusch, 2002; Timm et al., 2008). The modern calendar is commonly used in data-model comparisons (e.g., Harrison, 2013).

3 Results

3.1 Atmospheric circulation

The boreal winter (DFJ) 500 hPa heights in the PI simulation (Fig. 3a) display the observed high- and mid-latitude ridge-trough-ridge-trough standing wave structure (wave number two) that arises from continent-ocean-continent-ocean geography of the NH (Peixoto and Oort, 1992). From 21 ka to 9 ka the LIS, the FIS and Greenland ice sheets alter the NH standing wave structure resulting in persistent, distinct troughs and cyclonic flow tendencies over northeast Asia, the North Pacific, the continental interior of North America, the North Atlantic and Europe (Fig. 3, maps of raw fields SFig. 2).

Consistent with previous LGM studies using comparable (Braconnot et al., 2007a) and higher-resolution (Kim et al., 2007; Unterman et al., 2011) climate models, from 21 ka through 9 ka the western edge of the Cordilleran Ice Sheet diverts the LGM winter polar jetstream resulting in one branch that is weaker than PI over the Gulf of Alaska and the western and central regions of the ice sheet, and a second branch to the south of the ice sheet that is stronger than the PI (Fig. 3a). The reorganization creates westward wind anomalies over the North American Pacific Northwest. The LIS effectively guides the convergence of the branches, and the meridional gradient of low and high 500 hPa height anomalies in the North Atlantic intensifies flow over North America, the North Atlantic, Europe and Northern Africa (Figs. 3a) thereby altering the path of storm tracks. This flow pattern weakens progressively as the LIS recedes.

The influence of the NH ice sheets is also evident in summer (JJA), but to a lesser degree than in winter (Fig. 3b) due to continental heating and the absence of the strong, mid-latitude storm tracks. Between 21 ka and 15 ka, the summer jetstream is constrained and therefore enhanced along and to the south of the southern margin of the LIS extending over the North Atlantic. At 18 ka, a trend toward positive JJA anomalies in 500 hPa heights emerges over the regions of the semi-permanent subtropical high pressure of the North Pacific and central Atlantic. The regions of positive height anomalies, and their associated anticyclonic wind anomalies, expand over central North America, peak from 12 ka through 9 ka, and diminish by 6 ka (Fig. 3). The DJF pattern of low-to-high height anomalies over the North Atlantic is replaced during JJA by a strengthened subtropical high. Anticyclonic flow around positive height anomalies on the western edge of the FIS alters regional flow patterns over and south of the ice sheet. The GENMOM responses to the NH ice sheets are similar to many previous modeling experiments that have established that changes in tropospheric pressure–surface heights and winds are primarily driven by changes in ice-sheet height, and secondarily by temperature and albedo feedbacks (COHMAP Members, 1988; Felzer et al., 1996; 1998; Otto-Bliesner et al., 2006a; Pausata et al., 2011; Pollard and Thompson, 1997; Rind, 1987).

From 21 ka to 12 ka, the largest changes in boreal winter sea-level pressure (SLP) are associated with negative surface temperature anomalies over the continental ice sheets, the landmasses of the NH, and areas of expanded sea ice in the North Atlantic (Fig. 4a) where cooling increases subsidence and thus contributes to cold high surface pressure. From 21 ka to 15 ka, high pressure over the LIS produces anticyclonic flow across the northern Great Plains and over the Puget Lowlands of the US. Similar

anticyclonic tendencies are simulated along the margin of the FIS. Between 12 ka and 6 ka the winter SLP around the Aleutian low in the North Pacific and the Icelandic low in the North Atlantic is strengthened relative to PI. The Aleutian low is expanded southward whereas the Icelandic low is confined on the northern edge by the FIS and is slightly displaced southeastward.

From 21 ka to 9 ka, the JJA SLP anomalies remain strongly positive over the ice sheets and sea ice, whereas from 12 ka to 6 ka the SLP anomalies over Northern Hemisphere landmasses are negative due to enhanced continental warming (Fig. 4b). The patterns of the JJA 500 hPa heights, SLP and the associated circulation over North America and adjacent oceans again illustrate similar responses to time-varying controls: changes from 21 ka to 15 ka are primarily driven by changes in the LIS, whereas from 12 ka to 6 ka the circulation changes are related to the changes in the seasonality of Holocene NH insolation (Fig. 2).

3.2 Near-surface air temperature

Our time slice simulations clearly display surface air temperature (SAT) changes attributed to radiative forcing from the presence of the continental ice sheets, GHGs (Clark et al., 2012), and insolation (Fig. 5). The global average mean annual LGM temperature simulated by GENMOM is 3.8 °C colder than the PI (Table 2, Fig. 5a), within the range of cooling in the PMIP2 AOGCM simulations (3.1 °C to 5.6 °C and average 4.4 °C) and the PMIP3 simulations (2.6 °C to 5.0 °C and average of 4.4 °C) that were forced by similar boundary conditions (Harrison et al., 2013; Kageyama et al., 2006). Our LGM cooling is also in agreement with Annan and Hargreaves (2013), who reconciled the PMIP2 ensemble and proxy data to derive an estimated cooling of 4.0 ±

0.8 °C, but falls outside the range of Schmittner et al. (2011b) who found a median cooling of 3.0 ºC (66% probability range of 2.1 ºC - 3.3 ºC). GENMOM is also consistent with three transient simulations (Liu et al., 2014) averaged over the periods simulated by GENMOM. Excluding the BA and YD, our simulations reproduce the rate of warming between 21 ka and 15 ka, but are consistently ~1 °C colder than the reconstruction of Shakun et al. (2012) when sampled at the proxy sites (Fig. 5b). During these periods, GENMOM falls at the low end or outside the range of the transient models; however, GENMOM falls within the range of LGM and MH cooling simulated by the PMIP3 models, which have similar experimental designs and large scale boundary conditions.

Neither GENMOM nor the ensemble mean of the PMIP3 models capture the ~0.5 °C the 6 ka temperature anomaly in the Marcott et al. (2013) reconstruction. The change in the 6 ka mean annual temperature at the proxy sites in the 12 PMIP3 models we analyzed ranged from -0.3 to 0.3 °C with a mean of ~0.0 °C. Three models simulated slight warming, five near zero and four simulated slight cooling. Whether or not some proxies used in the temperature reconstructions have seasonal bias which would exaggerate the mid-Holocene warming remains an open research question (Liu et al., 2014).

Seasonal temperature changes across our time slice simulations illustrate the spatial and temporal effect of changing boundary conditions (Fig. 6). From 21 ka through 15 ka, both DJF and JJA exhibit cold temperature anomalies exceeding 16 °C over and adjacent to the ice sheets in both hemispheres. With the exception of Europe and the high latitudes of the NH, boreal winters remain generally colder than PI over the continents until 3 ka (Fig. 6), corresponding to reduced insolation. NH atmospheric circulation

changes induced by atmospheric blocking from the LIS (Fig. 3) sustain positive winter and summer temperature anomalies over Beringia. Summer warming also occurs south of the FIS across much of Asia. Although the mid-Holocene wintertime deficit in insolation is small at high northern latitudes, changes in short-wave radiation at the surface during boreal summer in the model are large and positive (30 – 40 Wm^{-2}) due to the precessional shift of perihelion and changes in obliquity (SFig. 4). Substantial warming occurs between most pairs of consecutive time slices from the LGM through the Holocene (Fig. 7, Table 2); however, over the African and Indian monsoon regions increased cloudiness associated with enhanced summer monsoonal precipitation leads to cooling from 15 to 6 ka.

The relatively high rate of warming between 18 ka and 15 ka (1.5 °C land and 0.5 °C ocean, Fig. 7, Table 2) is commensurate with increased GHGs (Table 1). Periods of peak annual warming from 15 ka to 12 ka (2.4 °C land and 0.7 °C ocean) and from 12 ka to 9 ka (1.6 °C land and 0.2 °C ocean) are associated with increasing GHG concentrations, ablation of the NH ice sheets (Figs. 1 and 6a). The simulated rates of annual global warming between the LGM and the early Holocene (Fig. 5) are in agreement with data (Clark et al., 2012; Gasse, 2000), and the analyses by Shakun et al. (2012) and Marcott et al. (2013) who attribute a large component of the warming to rising GHG levels.

The DJF and JJA temperature differences in our 21 ka simulation are similar to those of the PMIP3, allowing for differences in between our prescribed NH ice sheets (ICE-4G+OSU-LIS in GENMOM) and the blended ice sheet of the PMIP3 simulations that essentially combines the height of the ICE6G reconstruction with the extent of the

Dyke and Prest (1987) reconstructions (SFigs. 5 - 10, Braconnot et al., 2012). In both seasons, GENMOM produces 0.5 - 1 °C less cooling in the tropical oceans and greater warming over Beringia. The positive JJA temperature anomaly south of the FIS in GENMOM persists through 15 ka. Summer warming in the presence of the ice sheet was identified in earlier versions of GENESIS (Pollard and Thompson, 1997) and is associated with subsidence over the ice (Rind, 1987). Similar JJA warming also occurs in some of the PMIP3 models, but is likely a model artifact (Pollard and Thompson, 1997; Ramstein and Joussaume, 1995; Rind, 1987).

The DJF and JJA temperature anomalies in our 6 ka simulation are also similar to those of the PMIP3 models (SFigs. 7 and 8). Relative to PI, GENMOM produces slightly greater winter warming over Scandinavia than is evident in the average of the PMIP3 simulations, and is generally 0.5 - 1.0 °C cooler over Asia, Africa and South America. During boreal summer, GENMOM simulates warming over the NH landmasses and cooling over the North African and Indian monsoon regions, consistent with the PMIP3 models. Continental warming in GENMOM is ~ 0.5 - 1.0 °C weaker than most PMIP3 models, particularly in Europe and Asia. A portion of the weaker warming in GENMOM is attributed to the prescribed 6 ka GHG concentrations we derived from the ice-core data that differ slightly from those specified for the PMIP3 experiments (Table 1 caption).

3.3 Precipitation and monsoons

The simulated global precipitation anomalies display a progression from the drier and colder conditions of the LGM to the warmer and wetter conditions of the Holocene (Fig. 8, Table 2). The global mean annual precipitation change of -0.29 mm d^{-1} for the LGM is distributed as greater drying over land and ice sheets (-0.30 mm d^{-1}) than oceans

(-0.22 mm d^{-1}). Regionally coherent patterns of precipitation change (Figs. 8 and 9) are indicative of displacement and changes in the strength of storm tracks (Li and Battisti, 2008), the ITCZ and the Hadley circulation, and the onset, amplification and subsequent weakening of the global monsoons regions (Broccoli et al., 2006; Chiang, 2009; Chiang and Bitz, 2005).

Between the LGM and 15 ka, during DJF areas over and adjacent to the NH ice sheets display predominately reduced precipitation arising from a combination of the desertification-effect of the high and cold ice, lower-than-present atmospheric moisture and cloudiness and the advection of cold, dry air off of the ice sheets (Figs. 3a, 4a, 6a and 8a). The topographic and thermal effects of the LIS and the thermal effect of sea ice

(Kageyama et al., 1999; Li and Battisti, 2008) alter 500 hPa geopotential heights along the southern margin of the ice sheet (Figs. 3a and SFig. 2a), causing the development of positive precipitation anomalies extending from the eastern Pacific across the Gulf of Mexico, eastern North America and into the Northern Atlantic. Accompanying negative precipitation anomalies over the North Atlantic and positive anomalies over the Nordic Seas are related to changes in the location of storm tracks. The local effect of the ice sheets on precipitation diminishes during the early and mid-Holocene as their influence on circulation weakens and the atmosphere becomes warmer and moister (Fig. 9a).

The negative DJF anomalies that persist from 21 ka to 15 ka during austral summer along the equatorial and low-latitude areas of South and Central America, south-central Africa Southeast Asia, Northern Australia, the tropical Atlantic, the Indian Ocean and the western Pacific warm pool are caused by changes in the location of the ITCZ and

400 weakened southern monsoonal circulation. This particularly affects the winter monsoon
401 in central South America (Cheng et al., 2012; Zhao and Harrison, 2012) and in Southeast
402 Asia and Indonesia where additional feedbacks in the energy and water balances over
403 emergent land areas occur during low sea level stands (Figs. 1 and 8a) have been shown
404 to alter the Walker Circulation (DiNezio and Tierney, 2013).

405 Precipitation for JJA also exhibits considerable change over time (Figs. 8b and
406 9b). Similar to DJF, generally drier conditions are simulated over and adjacent to the NH
407 ice sheets where anticyclonic flow tendencies suppress precipitation (Fig. 4b). Along
408 portions of the southern margins of the LIS and FIS, however, orographic lifting
409 enhances precipitation at 21 ka (Pollard and Thompson, 1997). Wetter conditions in the
410 North American Southwest derive from enhanced westerly flow aloft and lower level
411 southwesterly flow off the eastern Pacific that are associated with displacement of the
412 jetstream by the ice sheets and the weakened Pacific subtropical high. Between 21 ka and
413 12 ka the LIS causes an increased pressure gradient from a strengthened Azores-Bermuda
414 high and weakened subtropical high in the eastern Pacific (Figs. 3b and 4b), resulting in
415 amplified and displaced westward winds, drying over Central America, and wetter-than-
416 present conditions over northern South America. At the LGM, North Africa, Europe, and
417 all but the western edge of Asia, are drier than the PI, again reflecting the drier
418 atmosphere of the full glacial.

419 The magnitude, gradients and spatial patterns of GENMOM 21 ka DJF
420 precipitation anomalies are consistent with the PMIP3 experiments. Notable exceptions
421 are greater drying than some models in the North Atlantic and the band of positive
422 anomalies extending across the Gulf of Mexico and the southeast US. GENMOM

423 produces positive precipitation anomalies over Australia, which is present in four of the
424 PMIP3 models. The 21 ka JJA precipitation anomalies are also in agreement with PMIP3,
425 but display weaker drying over eastern NA and slight drying over the North Africa
426 monsoon region.

427 The time evolution from LGM to PI of the African and Indian monsoons reflects
428 the interplay of changes in the location of the ITCZ and Hadley circulation that are linked
429 to the receding NH ice sheets, GHG-driven global warming, enhanced NH JJA insolation
430 and changing land-SST temperature contrast. The North Africa and Indian monsoons are
431 suppressed between 21 ka and 18 ka. After 18 ka, wetter-than-present conditions emerge
432 in the monsoon regions of North Africa and India where increased JJA insolation warms
433 the continents which amplifies the land-sea temperature contrasts that drive monsoonal
434 circulation (Braconnot et al., 2007b; Kutzbach and Otto-Bliesner, 1982; Zhao and
435 Harrison, 2012). The simulated DJF air temperatures in North Africa cool from the LGM
436 until 15 ka, and then warm monotonically through the rest of the deglaciation and
437 Holocene (Fig. 10). Wintertime precipitation over the North African region is minimal. In
438 contrast, JJA temperatures increase throughout the deglaciation, peak at 9 ka, decrease
439 slightly at 6 ka, and increase thereafter. A commensurate increase in JJA precipitation
440 over North Africa between 12 ka and 6 ka is associated with northward migration of the
441 ITCZ (Braconnot et al., 2007a; 2007b; Kutzbach and Liu, 1997), which enhances the
442 transport of moisture into both the North African and Indian monsoon regions.
443 Monsoonal precipitation peaks over both regions between 12 ka and 9 ka (Fig. 10). The
444 change in precipitation between 9 ka and 6 ka over India (0.9 mm d^{-1}) is nearly double
445 the change over North Africa (0.5 mm d^{-1}), consistent with the diagnoses of the mid-

Holocene monsoon of Marzin and Braconnot (2009) who attribute the stronger ~9 ka monsoon to insolation related to precession and snow cover on the Tibetan Plateau. The pattern of precipitation in the Indian monsoon region is similar to that of North Africa, but exhibits a greater range between peak Holocene values and the PI.

The overall temporal progression and magnitude of precipitation changes in the time slice simulations are in agreement with the PMIP2 (Braconnot et al., 2007a; 2007b) and PMIP3 simulations at 21 and 6 ka, and with other mid-Holocene modeling studies (Hély et al., 2009; Kutzbach and Liu, 1997; Kutzbach and Otto-Bliesner, 1982; Timm et al., 2010). More specifically, the June through September GENMOM precipitation anomaly of -0.6 mm d^{-1} over the North Africa monsoon region during the LGM is within the range (-0.9 to 0.1 mm d^{-1}) of 5 PMIP2 AOGCMs (Braconnot et al., 2007a) and 7 PMIP3 models (range of -0.6 to 0.2 and average of -0.2 mm d^{-1}). The GENMOM LGM anomaly over India (-0.9 mm d^{-1}) is also within the range (-1.7 to -0.1 mm d^{-1}) of the PMIP2 simulations (Braconnot et al., 2007a) and the PMIP3 simulations (range of -1.3 to 0.0 and average of -0.7 mm d^{-1}).

The northward expansion and spatial pattern of precipitation anomalies of the 6 ka monsoons are in very good agreement with both the PMIP2 and PMIP3 experiments. Summer precipitation in the GENMOM simulation is enhanced by 0.9 mm d^{-1} relative to PI over North Africa, in agreement with the range (0.2 to 1.4 mm d^{-1}) and mean (0.7 mm d^{-1}) of 11 PMIP2 AOGCMs (Zhao and Harrison, 2012) and 12 PMIP3 models (range of 0.1 to 1.0 and average of 0.6 mm d^{-1}). Over India, the 6 ka GENMOM precipitation anomaly of 1.1 mm d^{-1} exceeds the range (0.2 to 0.9 mm d^{-1}) and mean (0.6

468 mm d^{-1}) of the 11 PMIP2 models (Zhao and Harrison, 2012), but is within the range of
469 the PMIP3 models (0.5 to 1.3 and average of 1.0 mm d^{-1}) .

470 **3.4 Sea ice**

471 DJF sea ice is present in the PI simulation over Hudson Bay, the Arctic Ocean,
472 along the coast of eastern Canada, around Greenland, the Nordic Seas and the Baltic and
473 North Sea (Fig. 11), in agreement with observed present-day distributions (Jaccard et al.,
474 2005). Ice fractions of up to 100% are simulated over the Bering Sea and the Sea of
475 Okhotsk. In the SH, sea ice persists through austral summer in the Weddell and Ross
476 Seas and a few scattered locations around Antarctica. While the locations of the ice
477 around Antarctica are in agreement with observations (Gersonde et al., 2005), the model
478 underestimates the ice extent over the Weddell Sea and between the Weddell and Ross
479 Seas. The lack of ice is partly attributable to a warm bias in the Southern Ocean
480 associated with the previously mentioned weak ACC (discussed further below). During
481 August and September, simulated sea ice is greatly reduced in the North Atlantic region
482 (Fig. 11), with remnant ice persisting in the extreme north of Baffin Bay and the east
483 coast of Greenland, also in agreement with observations. In the SH, the corresponding
484 winter sea ice grows substantially and the distribution is in generally good agreement
485 with observations (Gersonde et al., 2005).

486 The simulated annual average ice extents for the NH are 9.8×10^6 km^2 for the
487 LGM, 15.8×10^6 km^2 for 6 ka and 14.1×10^6 km^2 for PI (grid cells with fractional coverage
488 > 15%). Compounded with climate-forcing, changes in both the distribution and areal
489 coverage of the NH ice also reflect the change in ocean area due to the transition of land
490 and ice sheets to ocean as sea level rises (Fig. 11 and SFigs. 13 - 15). For the same time

491 periods, the SH ice area extents, which are minimally affected by land-sea transitions with
492 sea level rise, are 20.9×10^6 km^2, 11.4×10^6 km^2 and 11.1×10^6 km^2, respectively.

493 During the 21 ka boreal winter, the Arctic Ocean and Baffin Bay are fully covered
494 by ice and the ice around Greenland expands. The model displays increased sea ice in the
495 western North Atlantic and decreased ice in the eastern North Atlantic and Nordic Seas
496 where the prescribed FIS margin advances into the water (Fig. 2). The limit of substantial
497 coverage north of 55°N is in agreement with reconstructions (de Vernal et al., 2006) and
498 other LGM simulations (Otto-Bliesner et al., 2006a; Roche et al., 2007); however, slight
499 fractional cover (pack ice) in the model likely extends too far south (to ~45°N) along the
500 coast of North America. Fractional cover of up to 100% is simulated in the far Northwest
501 Pacific and the Sea of Okhotsk with a sharp, southward transition to reduced coverage. In
502 boreal summer of the LGM, simulated sea ice retreats to 65°N in the North Atlantic and
503 persists along eastern Canada, Baffin Bay and south of Greenland and the extreme
504 northern areas of the Nordic Seas.

505 The overall distribution of SH sea ice (Fig. 11) is in good agreement with
506 reconstructions and other model simulations (Gersonde et al., 2005; Roche et al., 2012).
507 The simulated LGM maximum winter sea ice area is 35.5×10^6 km^2 (72% greater than PI)
508 and the LGM summer minimum is 4.8×10^6 km^2 (112% greater than PI); the winter and
509 summer reconstructed areas are $43.5 \pm 4\times10^6$ km^2 and $11.1 \pm 4\times10^6$ km^2, respectively
510 (Roche et al., 2012). The seasonal amplitude (maximum minus minimum) of LGM ice
511 cover simulated by GENMOM (30.6×10^6 km^2) is comparable with the reconstructed
512 amplitude ($32.4 \pm 4\times10^6$ km^2) and the LGM-to-PI change of seasonality is well within the
513 range simulated by the PMIP2 models (Roche et al., 2012 their Figures 2 and 3).

3.5 Antarctic Circumpolar Current and Atlantic Meridional Overturning Circulation

The simulated ACC of 62 Sv is ~48% weaker than the observed value of 119 Sv through the Drake Passage (GECCO data; Köhl and Stammer, 2008). Although the T31 resolution of GENMOM is a factor in limiting flow through the Drake Passage, we attribute the underestimate of the ACC in part to insufficient wind stress at the latitude of the Drake Passage, which is caused by equatorward displacement of the core of the westerly winds, a shortcoming in common with other low-resolution AOGCMs (Alder et al., 2011; Russell et al., 2006; Schmittner et al., 2011a).

Considerable uncertainty exists in the proxies that are used to infer past changes in AMOC strength (Delworth and Zeng, 2008; Lynch-Stieglitz et al., 2007). The $^{231}Pa/^{230}Th$ record from 33°N on the Bermuda Rise (Lippold et al., 2009; McManus et al., 2004) indicates that after the LGM the strength of the AMOC began to diminish at ~18 ka, was further reduced during Heinrich Event 1 (H1) at ~17 ka, increased abruptly during the BA at 15 ka, and weakened again during the YD cold reversal at ~12 ka. After the YD, the AMOC strengthened again and stabilized. In climate models, a variety of factors including the North Atlantic freshwater budget, model resolution and parameterizations and the characteristics of simulated Antarctic Bottom Water (AABW) give rise to a considerable simulated range of AMOC (Weber et al., 2007).

The AMOC in our PI simulation (Fig. 12) is 19.3 ± 1.4 Sv at the core site of 33°N, a value similar to the present-day estimate of 18.7 ± 4.8 Sv at 26.5°N (Srokosz et al., 2012). The maximum AMOC simulated by GENMOM in the PI is 21.3 Sv at 41°N, a value outside the range of 13.8 to 20.8 Sv of five models in the PMIP2 experiments (Weber et al., 2007), but within the range of 3.8 to 31.7 Sv of the IPCC AR4

538 models (Meehl et al., 2007; Schmittner et al., 2005). The newer CMIP5 models have a
539 narrower range of AMOC of ~14 to ~30 Sv when sampled at 30°N (Cheng et al., 2013);
540 GENMOM simulates 16.0 ± 1.3 Sv at this location.

541 Our simulated LGM AMOC at the core site is 16.4 Sv, which is a ~14.7%
542 reduction relative to the PI. The maximum LGM AMOC is 22.4 Sv at 40.8°N, an
543 increase of 1.1 Sv (5.1%) relative to the PI maximum and within the considerable range
544 of -6.2 to +7.3 Sv in five PMIP2 simulations (Weber et al., 2007). In the deglacial
545 simulations (21 ka through 15 ka), the northward (positive) AMOC flow extends deeper
546 than that of the PI (Fig. 12) and the southward flow or AABW consequently is somewhat
547 weakened. The maximum AMOC in GENMOM is essentially constant at 40.8°N depth
548 of 1.23 km for all time slices. Although the depth of the maximum is again comparable to
549 the range of the PMIP2 models (1.24 ± 0.20), the invariance of the location and depth in
550 GENMOM is likely a model-specific response.

551 Our time slice simulations display an increase in the strength of AMOC from the
552 LGM to a maximum at 15 ka, decrease to a minimum at 9 ka, and remain more-or-less
553 constant through the PI (Fig. 13), which is in apparent disagreement with the $^{231}Pa/^{230}Th$
554 records from which greater variability is inferred (Lippold et al., 2009; McManus et al.,
555 2004). We do not expect to capture rapid and abrupt climate change events such as H1
556 (~17 ka), the BA (~15 ka) and the YD (~12 ka) with only eight time slices, because we
557 did not manipulate freshwater discharge to the North Atlantic in our experimental design.

558 ## 4 21 ka and 6 ka data-model comparisons

559 We compare temperature and precipitation from our LGM and mid-Holocene
560 simulations with paleoclimatic reconstructions and the PMIP3 simulations. For the LGM,

we use the pollen-based reconstructions of mean annual mean temperature (MAT) and precipitation (MAP) from Bartlein et al. (2011) over land, and the Multiproxy Approach for the Reconstruction of the Glacial Ocean Surface Project (MARGO) reconstructions over oceans (Waelbroeck et al., 2009). The gridded 2° x 2° pollen data include >3,000 terrestrial pollen records from Eurasia, Africa and North America, and the global MARGO reconstruction comprises ~700 analyses of planktonic foraminifera, diatom, dinoflagellate cyst and radiolarian abundances, alkenones, and planktonic foraminifera Mg/Ca from marine core sites. For 6 ka, we combine the pollen-based reconstructions of Bartlein et al. (2011) and the GHOST SST reconstructions (Leduc et al., 2010). The 6 ka GHOST data set contains ~100 reconstructed temperature records based on analyses of alkenones and foraminifera Mg/Ca from marine sites located along continental margins and the Mediterranean Sea.

4.1 21 ka

Our simulated 21 ka anomalies of MAT and MAP are comparable with the pollen reconstructions (Fig. 14) and fall within the range of the PMIP3 models. GENMOM captures the mixed pattern of temperature and precipitation anomalies over Beringia that are present in the reconstructions (Fig. 14a,b) and in several of the PMIP3 simulations (SFigs. 8, 9, and 16). The GENMOM SST anomalies indicate broad cooling of the global oceans (mean of -1.7 °C) but not as much cooling as is simulated in the PMIP3 models (mean of -2.9 °C); although, Harrison et al. (2013) found that the PMIP3 models tended to overestimate oceanic cooling. Sampled at the MARGO locations, GENMOM is generally warmer, but within the range of the PMIP3 models (Harrison et al., 2013). The overall agreement of the simulation with the MARGO data is good, but some features in

584 the MARGO data are not reproduced by GENMOM. For example, similar to the PMIP3
585 simulations (SFigs. 5, 6 and 16) the GENMOM simulation lacks the warming over the
586 Greenland and Nordic Seas inferred from the data; although, while the data indicate the
587 Nordic Sea was ice free at the LGM, the magnitude of the warming elsewhere, if it
588 occurred, is somewhat unclear (de Vernal et al., 2006; Moller et al., 2013). The limited
589 cooling along the western coast of North America and Mediterranean in GENMOM is
590 attributed to the inability of the model to resolve the California Current and the
591 Mediterranean circulation (Alder et al., 2011).

592 Over the tropical ocean basins, the 21 ka GENMOM simulation is 1.6 °C colder
593 than the PI, in good agreement with the inferred MARGO cooling of 1.7 ± 1 °C (Otto-
594 Bliesner et al., 2009). Average simulated SST anomalies are also similar to MARGO
595 over the Indian (-1.6 °C versus -1.4 ± 0.7 °C) and Pacific (-1.5 °C versus -1.2 ± 1.1 °C)
596 Oceans, but are warmer than the data in the tropical Atlantic basin (-1.9 °C versus -2.9 ±
597 1.3 °C). In each of these regions, the anomalies simulated by GENMOM fall within the
598 range of six PMIP2 models analyzed by Otto-Bliesner et al. (2009). GENMOM captures
599 the 2 – 4 °C cooling in the eastern coastal Atlantic evident in the MARGO data, and the
600 SST anomalies are ~2 – 4 °C colder over the Western Pacific Warm Pool. Neither
601 GENMOM nor the PMIP3 simulations produce the warming over the central and eastern
602 tropics, or the low latitudes and the North Atlantic that is evident in the MARGO
603 reconstruction.

604 The simulated LGM MAP anomalies are also comparable with the pollen-based
605 reconstructions (Fig. 14c and d). The model simulates general drying of the NH and a
606 mix of increased and decreased precipitation in Beringia, South America, southern

607 Africa, Southeast (SE) Asia and Australia. GENMOM produces strong drying over and
608 around the NH ice sheets, wetter-than-present conditions in the southwestern United
609 States and drying in Central America. The simulation fails to reproduce the drying over
610 eastern North America that is inferred from the pollen-based data. There is considerable
611 variability in the PMIP3 simulations of MAP (SFigs. 9 and 10). In common with the
612 PMIP3 models, GENMOM simulates a general reduction of precipitation over the NH,
613 the North African and Indian monsoon regions, and SE Asia, and increased precipitation
614 south of the LIS, southern Africa and much of Australia (SFig. 16).

615 **4.2 6 ka**

616 Relative to PI, the changes in 6 ka boundary conditions are predominantly in the
617 seasonality of insolation (Table 1) as opposed to the stronger radiative forcing associated
618 with changes in GHGs and continental ice sheets from the LGM through the early
619 Holocene. The resulting changes in 6 ka climatology are thus more subtle than those of
620 the deglaciation. The changes of 6 ka MAT simulated by GENMOM are generally within
621 the range of ±1 °C (Fig. 15b). Enhanced MAP and associated cooling are evident in the
622 NH monsoonal regions (Fig. 15d). Elsewhere, MAP changes are within a range of
623 ±50 mm.

624 Pollen-based data reconstructions indicate highly heterogeneous changes in MAT
625 during 6 ka; however, there are regions with spatially consistent changes in sign, such as
626 warming south of Hudson Bay, areas of warming over Scandinavia and Western Europe,
627 and cooling in the Mediterranean region (Fig. 15a). Larger MAT changes at high-
628 elevation sites and regions with anomalies of mixed sign occur in the data over most
629 continents. The GENMOM 6 ka MAT anomalies also display a mix of warming and

630 cooling in a range of about ±4 °C; however, where pollen-based records exist, the
631 majority of the anomalies are within a narrower range of about ±1.5 °C (Fig. 15b).
632 GENMOM, and many of the PMIP3 models (SFigs. 8, 9 and 16), produce a mixture of
633 warm and cold 6 ka MAT anomalies that are generally in the range of ±1 °C over the
634 North Atlantic, Europe and Scandinavia, which underestimates the proxy-based
635 anomalies by >2 °C at some sites.

636 The Asian pollen-based reconstruction similarly displays a heterogeneous
637 temperature pattern that is reproduced by GENMOM and the PMIP3 models. In all of the
638 models, the sign of the anomalies does not vary abruptly in close proximity to the pollen
639 sites. We note, however, that the smooth topography in GCMs limits the ability of the
640 models to reproduce large and regionally spatially heterogeneous anomalies that are
641 characteristic of the local climate at many high elevation pollen sites in Western North
642 America, the Alps, the central plateau of African and Asia.

643 GENMOM displays cooling in the North African and Indian monsoon regions
644 and warming over the high northern latitudes, consistent with the PMIP3 models (Fig.
645 15). In contrast, GENMOM simulates weak global cooling of 0.39 °C compared to no
646 change in the PMIP3 model average which is partially attributed to our lower prescribed
647 GHG concentrations (Table 1 caption).

648 Precipitation anomalies inferred from the pollen-based data indicate that 6 ka was
649 wetter than the PI in Europe, Africa, Asia and some parts of western North America and
650 drier than PI in much of eastern North America and Scandinavia (Fig. 15c). GENMOM
651 simulates the gradients and coherent patterns of positive and negative MAP anomalies
652 over North America, and North, Central and western Africa, in agreement with the data

and the PMIP3 models. The data and GENMOM are also in agreement over the Asian monsoon region and northwest Asia where wetter conditions prevail, but anomalies of opposite sign are simulated over the Great Lowland Plain in north central Eurasia and Southeast Asia. Bartlein et al. (2011) attribute cooling in Southeast Asia to a stronger winter monsoon at 6 ka. Our results (Figs. 6a and 8a), and many of the PMIP3 models, indicate cooler, drier winters (SFigs. 7 and 11) and regionally variable changes in the summer (SFigs. 8 and 12).

In Africa, the model captures the increase in precipitation in the northern and continental regions and drying along the southern coastal regions, as evident in the data. Strengthening of the African and Indian summer monsoons during the mid-Holocene corresponds well with the PMIP2 and PMIP3 models (Zheng and Braconnot, 2013). Both GENMOM and the data indicate drying over central Scandinavia, wetter conditions over east central Europe, the Iberian Peninsula and around the Mediterranean but, over Western Europe, the simulated decrease in MAP in GENMOM clearly disagrees with the data and some of the PMIP3 models (Figs. 15, SFigs. 7, 8 and 16); although, the magnitude of the change in the models is very small and the sign of the change varies among models. Wetter conditions also prevail in Indonesia, and a southwest-to-northeast wet-dry gradient is simulated over Australia.

5 Summary

We have presented a suite of multi-century equilibrium climate simulations with GENMOM for the past 21,000 years at 3,000-yr intervals. Each 1,100-yr simulation was forced with fixed, time-appropriate global boundary conditions that included insolation, GHGs, continental ice sheets and adjustment for sea level. The key drivers of climate

676 change from the LGM through the Holocene are retreat of the NH ice sheets, deglacial
677 increased of GHG concentrations, and latitudinal and seasonal variations in insolation.

678 GENMOM reproduces reasonably well the LGM to Holocene temperature trends
679 inferred from the paleoclimate data syntheses of Shakun et al. (2012) and Marcott et al.
680 (2013). The evolution of global temperature change simulated by GENMOM is
681 consistent with three transient simulations, but is generally cooler during the deglacial
682 time slices than the transient simulations when sampled at the proxy locations. The global
683 LGM cooling of 3.8 °C simulated by GENMOM is within the range of 2.6 to 5.0 °C and
684 average of 4.4 °C simulated by the PMIP3 models. Simulated LGM cooling of the
685 tropical oceans is 1.6 °C, which is in good agreement with the MARGO reconstruction of
686 1.7 ± 1 °C. The weaker LGM global cooling is attributed to the sensitivity of GENMOM
687 to CO_2 (2.2 °C for a 2X increase in the present-day value).

688 During the LGM, simulated precipitation is reduced globally by 8.2% and
689 gradually increases through the Holocene to present-day values in response to loss of the
690 NH ice sheets, global warming and related increases in atmospheric humidity. Between
691 15 ka and 6 ka seasonal changes in insolation altered the NH land-sea temperature
692 contrasts, which, combined with shifts in global circulation, strengthened the summer
693 monsoons in Africa and India. Monsoonal precipitation in both regions peaked between
694 12 ka and 9 ka, consistent with pollen-based reconstructions. The spatial patterns of mid-
695 Holocene precipitation change simulated by GENMOM correspond well with the PMIP3
696 models, as do the 6 ka changes in monsoonal precipitation. In contrast to the pollen-based
697 reconstructions, GENMOM simulates slightly drier instead of slightly wetter-than-
698 present in Western Europe.

699 The eight time slice simulations depict the glacial-interglacial transition that is in
700 good agreement with other AOGCM simulations and compares reasonably well with
701 data-based climate reconstructions. The simulations provide insights into key dynamic
702 features of the transition, such as altered NH storm tracks and strengthening of monsoons
703 during the early to mid-Holocene. The data-model and model-model comparisons give us
704 a measure of confidence that our paleo GENMOM simulations are reasonable on broad
705 spatial scales and adds to the growing number of climate models that are capable of
706 simulating key aspects of past climate change when constrained by a relatively small set
707 of global boundary conditions. Future work using the model output produced by this
708 study will address how internal model variability and multidecadal variability influence
709 comparison with proxy data, particularly in North America using dynamical downscaling
710 techniques.

Appendix A: List of abbreviations and acronyms

AABW	Antarctic Bottom Water
ACC	Antarctic Circumpolar Current
AMOC	Atlantic Meridional Overturning Circulation
AOGCM	Atmosphere-Ocean General Circulation Model
BA	Bølling-Allerød
CIS	Cordilleran Ice Sheet
CLIMAP	Climate: Long range Investigation, Mapping, and Prediction
COHMAP	Cooperative Holocene Mapping Project
DJF	December, January and February
FIS	Fennoscandian Ice Sheet
GECCO	German partner of Estimating the Circulation and Climate of the Ocean
GENESIS	Global Environmental and Ecological Simulation of Interactive Systems
GHG	Greenhouse gas
ITCZ	Intertropical Convergence Zone
H1	Heinrich Event 1
JJA	June, July and August
LGM	Last Glacial Maximum
LIS	Laurentide Ice Sheet
LSX	Land Surface eXchange
MAM	March, April and May
MAP	Mean annual precipitation
MARGO	Multiproxy Approach for the Reconstruction of the Glacial Ocean Surface Project
MAT	Mean annual temperature
MOM2	Modular Ocean Model version 2
NCAR	National Center for Atmospheric Research
NCEP	National Centers for Environmental Prediction
NH	Northern Hemisphere
OSU-LIS	Oregon State University Laurentide Ice Sheet
PD	Present-day
PI	Pre-industrial
PMIP	Palaeoclimate Modelling Intercomparison Project
SH	Southern Hemisphere
SLP	Sea-level pressure
SON	September, October and November
SST	Sea surface temperature
TEMPO	Testing Earth System Models with Paleoenvironmental Observations
YD	Youger Dryas

750 ## Acknowledgments

751 We thank P. Bartlein, J. Shakun, S. Marcott, the MARGO and GHOST project
752 members for providing their proxy reconstructions. Z. Liu and J. Zhu kindly provided
753 time series data for the three transient models CCSM3, LOVECLIM and FAMOUS. We
754 thank P. Bartlein, D. Pollard and R. Thompson for their thoughtful reviews and A.
755 Schmittner, S. Marcott and P. Clark for helpful discussions and insights.

756

References

Alder, J. R., Hostetler, S. W., Pollard, D. and Schmittner, A.: Evaluation of a present-day climate simulation with a new coupled atmosphere-ocean model GENMOM, Geosci. Model Dev., 4(1), 69–83, doi:10.5194/gmd-4-69-2011, 2011.

Annan, J. D. and Hargreaves, J. C.: A new global reconstruction of temperature changes at the Last Glacial Maximum, Clim Past, 9(1), 367–376, doi:10.5194/cp-9-367-2013, 2013.

Bartlein, P. J., Harrison, S. P., Brewer, S., Connor, S., Davis, B. A. S., Gajewski, K., Guiot, J., Harrison-Prentice, T. I., Henderson, A., Peyron, O., Prentice, I. C., Scholze, M., Seppä, H., Shuman, B., Sugita, S., Thompson, R. S., Viau, A. E., Williams, J. and Wu, H.: Pollen-based continental climate reconstructions at 6 and 21 ka: a global synthesis, Clim Dynam, 37(3-4), 775–802, doi:10.1007/s00382-010-0904-1, 2011.

Beckmann, B., Flogel, S., Hofmann, P., Schulz, M. and Wagner, T.: Orbital forcing of Cretaceous river discharge in tropical Africa and ocean response, Nature, 437(7056), 241–244, doi:10.1038/nature03976, 2005.

Berger, A. and Loutre, M. F.: Insolation values for the climate of the last 10 million years, Quaternary Sci Rev, 10(4), 297–317, doi:10.1016/0277-3791(91)90033-Q, 1991.

Bice, K. L., Birgel, D., Meyers, P. A., Dahl, K. A., Hinrichs, K.-U. and Norris, R. D.: A multiple proxy and model study of Cretaceous upper ocean temperatures and atmospheric CO2 concentrations, Paleoceanography, 21(2), PA2002, doi:10.1029/2005PA001203, 2006.

Braconnot, P., Harrison, S. P., Kageyama, M., Bartlein, P. J., Masson-Delmotte, V., Abe-Ouchi, A., Otto-Bliesner, B. L. and Zhao, Y.: Evaluation of climate models using palaeoclimatic data, Nat Geosci, 2(6), 417–424, doi:10.1038/nclimate1456, 2012.

Braconnot, P., Otto-Bliesner, B. L., Harrison, S., Joussaume, S., Peterschmitt, J. Y., Abe-Ouchi, A., Crucifix, M., Driesschaert, E., Fichefet, T., Hewitt, C. D., Kageyama, M., Kitoh, A., Laîné, A., Loutre, M. F., Marti, O., Merkel, U., Ramstein, G., Valdes, P., Weber, S. L., Yu, Y. and Zhao, Y.: Results of PMIP2 coupled simulations of the Mid-Holocene and Last Glacial Maximum - Part 1: experiments and large-scale features, Clim Past, 3(2), 261–277, 2007a.

Braconnot, P., Otto-Bliesner, B. L., Harrison, S., Joussaume, S., Peterschmitt, J. Y., Abe-Ouchi, A., Crucifix, M., Driesschaert, E., Fichefet, T., Hewitt, C. D., Kageyama, M., Kitoh, A., Loutre, M. F., Marti, O., Merkel, U., Ramstein, G., Valdes, P., Weber, L., Yu, Y. and Zhao, Y.: Results of PMIP2 coupled simulations of the Mid-Holocene and Last Glacial Maximum - Part 2: feedbacks with emphasis on the location of the ITCZ and mid- and high latitudes heat budget, Clim Past, 3(2), 279–296, 2007b.

793 Broccoli, A. J., Dahl, K. A. and Stouffer, R. J.: Response of the ITCZ to Northern
794 Hemisphere cooling, Geophys. Res. Lett., 33(1), L01702,
795 doi:10.1029/2005GL024546, 2006.

796 Brohan, P., Kennedy, J. J., Harris, I., Tett, S. F. B. and Jones, P. D.: Uncertainty
797 estimates in regional and global observed temperature changes: A new data set from
798 1850, J.-Geophys.-Res., 111(D12), doi:10.1029/2005JD006548, 2006.

799 Brook, E. J., Harder, S., Severinghaus, J., Steig, E. J. and Sucher, C. M.: On the origin
800 and timing of rapid changes in atmospheric methane during the last glacial period,
801 Global Biogeochem Cy, 14(2), 559–572, 2000.

802 Cheng, H., Sinha, A., Wang, X., Cruz, F. W. and Edwards, R. L.: The Global
803 Paleomonsoon as seen through speleothem records from Asia and the Americas, Clim
804 Dynam, 39(5), 1045–1062, doi:10.1007/s00382-012-1363-7, 2012.

805 Cheng, W., Chiang, J. C. H. and Zhang, D.: Atlantic Meridional Overturning Circulation
806 (AMOC) in CMIP5 Models: RCP and Historical Simulations, J Climate, 26(18),
807 7187–7197, doi:10.1175/JCLI-D-12-00496.1, 2013.

808 Chiang, J. C. H.: The Tropics in Paleoclimate, Annual Review of Earth and Planetary
809 Sciences, 37, 263–297, doi:10.1146/annurev.earth.031208.100217, 2009.

810 Chiang, J. C. H. and Bitz, C. M.: Influence of high latitude ice cover on the marine
811 Intertropical Convergence Zone, Clim Dynam, 25(5), 477–496, doi:10.1007/s00382-
812 005-0040-5, 2005.

813 Clark, P. U., Shakun, J. D., Baker, P. A., Bartlein, P. J., Brewer, S., Brook, E., Carlson,
814 A. E., Cheng, H., Kaufman, D. S., Liu, Z. Y., Marchitto, T. M., Mix, A. C., Morrill,
815 C., Otto-Bliesner, B. L., Pahnke, K., Russell, J. M., Whitlock, C., Adkins, J. F., Blois,
816 J. L., Clark, J., Colman, S. M., Curry, W. B., Flower, B. P., He, F., Johnson, T. C.,
817 Lynch-Stieglitz, J., Markgraf, V., McManus, J., Mitrovica, J. X., Moreno, P. I. and
818 Williams, J. W.: Global climate evolution during the last deglaciation, P Natl Acad
819 Sci USA, 109(19), E1134–E1142, doi:10.1073/Pnas.1116619109, 2012.

820 Claussen, M.: Late Quaternary vegetation-climate feedbacks, Clim Past, 5(2), 203–216,
821 doi:10.5194/cp-5-203-2009, 2009.

822 CLIMAP Project Members: Seasonal reconstructions of the earth's surface at the Last
823 Glacial Maximum, Geological Society of America, Map and Chart Series(MC-36),
824 1981.

825 COHMAP Members: Climatic Changes of the Last 18,000 Years - Observations and
826 Model Simulations, Science, 241(4869), 1043–1052, 1988.

827 de Vernal, A., Rosell-Mele, A., Kucera, M., Hillaire-Marcel, C., Eynaud, F., Weinelt, M.,
828 Dokken, T. and Kageyama, M.: Comparing proxies for the reconstruction of LGM

829 sea-surface conditions in the northern North Atlantic, Quaternary Sci Rev, 25(21-22),
830 2820–2834, doi:10.1016/j.quascirev.2006.06.006, 2006.

831 DeConto, R. M., Pollard, D. and Harwood, D.: Sea ice feedback and Cenozoic evolution
832 of Antarctic climate and ice sheets, Paleoceanography, 22(3), PA3214,
833 doi:10.1029/2006PA001350, 2007.

834 DeConto, R. M., Pollard, D., Wilson, P. A., Palike, H., Lear, C. H. and Pagani, M.:
835 Thresholds for Cenozoic bipolar glaciation, Nature, 455(7213), 652–656,
836 doi:10.1038/nature07337, 2008.

837 Delworth, T. L. and Zeng, F.: Simulated impact of altered Southern Hemisphere winds on
838 the Atlantic Meridional Overturning Circulation, Geophys. Res. Lett., 35(20),
839 L20708, doi:10.1029/2008gl035166, 2008.

840 DiNezio, P. N. and Tierney, J. E.: The effect of sea level on glacial Indo-Pacific climate,
841 Nature Geoscience, 6(6), 1–7, doi:10.1038/ngeo1823, 2013.

842 Dorman, J. L. and Sellers, P. J.: A Global Climatology of Albedo, Roughness Length and
843 Stomatal-Resistance for Atmospheric General-Circulation Models as Represented by
844 the Simple Biosphere Model (Sib), J Appl Meteorol, 28(9), 833–855,
845 doi:10.1175/1520-0450(1989)028<0833:Agcoar>2.0.Co;2, 1989.

846 Dyke, A. S. and Prest, V. K.: Late Wisconsinan and Holocene history of the Laurentide
847 ice sheet, Géographie physique et Quaternaire, 1987.

848 Felzer, B.: Climate impacts of an ice sheet in East Siberia during the Last Glacial
849 Maximum, Quaternary Sci Rev, 20(1-3), 437–447, doi:10.1016/S0277-
850 3791(00)00106-2, 2001.

851 Felzer, B., Oglesby, R. J., Webb, T. and Hyman, D. E.: Sensitivity of a general
852 circulation model to changes in northern hemisphere ice sheets, J.-Geophys.-Res.,
853 101(D14), 19077–19092, 1996.

854 Felzer, B., Webb, T. and Oglesby, R. J.: The impact of ice sheets, CO2, and orbital
855 insolation on late quaternary climates: Sensitivity experiments with a general
856 circulation model, Quaternary Sci Rev, 17(6-7), 507–534, doi:10.1016/S0277-
857 3791(98)00010-9, 1998.

858 Flato, G. M. and Hibler, W. D.: Modeling Pack Ice as a Cavitating Fluid, J. Phys.
859 Oceanogr., 22(6), 626–651, 1992.

860 Gasse, F.: Hydrological changes in the African tropics since the Last Glacial Maximum,
861 Quaternary Sci Rev, 19(1-5), 189–211, doi:10.1016/S0277-3791(99)00061-X, 2000.

862 Gates, W. L. and Nelson, A. B.: A new (revised) tabulation of the Scripps topography on
863 a 1 degree global grid. Part 1: Terrain heights, Tech. Rep. R-1276-1-ARPA. 1975.

Gent, P. R. and Mcwilliams, J. C.: Isopycnal Mixing in Ocean Circulation Models, J. Phys. Oceanogr., 20(1), 150–155, doi:10.1175/1520-0485(1990)020<0150:IMIOCM>2.0.CO;2, 1990.

Gersonde, R., Crosta, X., Abelmann, A. and Armand, L.: Sea-surface temperature and sea ice distribution of the Southern Ocean at the EPILOG Last Glacial Maximum—a circum-Antarctic view based on siliceous microfossil records, Quaternary Sci Rev, 24(7-9), 869–896, doi:10.1016/j.quascirev.2004.07.015, 2005.

Harrison, S. P., Bartlein, P. J., Brewer, S., Prentice, I. C., Boyd, M., Hessler, I., Holmgren, K., Izumi, K. and Willis, K.: Climate model benchmarking with glacial and mid-Holocene climates, Clim Dynam, 1–18, doi:10.1007/s00382-013-1922-6, 2013.

Harvey, L. D. D.: Development of a Sea Ice Model for Use in Zonally Averaged Energy Balance Climate Models, J Climate, 1(12), 1221–1238, 1988.

Hassol, S. J.: Impacts of a Warming Arctic - Arctic Climate Impact Assessment, Impacts of a Warming Arctic - Arctic Climate Impact Assessment, by Arctic Climate Impact Assessment, pp. 144. ISBN 0521617782. Cambridge, UK: Cambridge University Press, December 2004., -1, 2004.

Hély, C., Braconnot, P., Watrin, J. and Zheng, W.: Climate and vegetation: Simulating the African humid period, Comptes Rendus Geoscience, 341(8-9), 671–688, doi:10.1016/j.crte.2009.07.002, 2009.

Horton, D. E., Poulsen, C. J. and Pollard, D.: Orbital and CO2 forcing of late Paleozoic continental ice sheets, Geophys. Res. Lett., 34(19), L19708, doi:10.1029/2007GL031188, 2007.

Hostetler, S. W., Clark, P. U., Bartlein, P. J., Mix, A. C. and Pisias, N. J.: Atmospheric transmission of North Atlantic Heinrich events, J.-Geophys.-Res., 104(D4), 3947–3952, 1999.

Hostetler, S. W., Pisias, N. and Mix, A. C.: Sensitivity of Last Glacial Maximum climate to uncertainties in tropical and subtropical ocean temperatures, Quaternary Sci Rev, 25(11-12), 1168–1185, doi:10.1016/j.quascirev.2005.12.010, 2006.

Jaccard, S. L., Haug, G. H., Sigman, D. M., Pedersen, T. F., Thierstein, H. R. and Rohl, U.: Glacial/interglacial changes in subarctic North Pacific stratification, Science, 308(5724), 1003–1006, doi:10.1126/science.1108696, 2005.

Joussaume, S., Taylor, K. E., Braconnot, P., mitchell, J., Kutzbach, J. E., Harrison, S. P., Prentice, I. C., Broccoli, A. J., Abe-Ouchi, A., Bartlein, P. J., Bonfils, C., Dong, B., Guiot, J., Herterich, K., Hewitt, C. D., Jolly, D., Kim, J. W., Kislov, A., Kitoh, A., Loutre, M. F., Masson, V., McAvaney, B., McFarlane, N., de Noblet, N., Peltier, W. R., Peterschmitt, J. Y., Pollard, D., Rind, D., Royer, J. F., Schlesinger, M. E., Syktus, J., Thompson, S. L., Valdes, P., Vettoretti, G., Webb, R. S. and Wyputta, U.:

902 Monsoon changes for 6000 years ago: Results of 18 simulations from the
903 Paleoclimate Modeling Intercomparison Project (PMIP), Geophys. Res. Lett., 26(7),
904 859–862, 1999.

905 Kageyama, M., D'Andrea, F., Ramstein, G., Valdes, P. J. and Vautard, R.: Weather
906 regimes in past climate atmospheric general circulation model simulations, Clim
907 Dynam, 15(10), 773–793, doi:10.1007/S003820050315, 1999.

908 Kageyama, M., Laîné, A., Abe-Ouchi, A., Braconnot, P., Cortijo, E., Crucifix, M., de
909 Vernal, A., Guiot, J., Hewitt, C. D. and Kitoh, A.: Last Glacial Maximum
910 temperatures over the North Atlantic, Europe and western Siberia: a comparison
911 between PMIP models, MARGO sea–surface temperatures and pollen-based
912 reconstructions, Quaternary Sci Rev, 25(17-18), 2082–2102,
913 doi:10.1016/j.quascirev.2006.02.010, 2006.

914 Kalnay, E., Kanamitsu, M., Kistler, R., Collins, W., Deaven, D., Gandin, L., Iredell, M.,
915 Saha, S., White, G., Woollen, J., Zhu, Y., Chelliah, M., Ebisuzaki, W., Higgins, W.,
916 Janowiak, J., Mo, K. C., Ropelewski, C., Wang, J., Leetmaa, A., Reynolds, R., Jenne,
917 R. and Joseph, D.: The NCEP/NCAR 40-year reanalysis project, Bull. Amer. Meteor.
918 Soc., 77(3), 437–471, 1996.

919 Kiehl, J. T., Hack, J. J., Bonan, G. B., Boville, B. A., Williamson, D. L. and Rasch, P. J.:
920 The National Center for Atmospheric Research Community Climate Model: CCM3, J
921 Climate, 11(6), 1131–1149, 1998.

922 Kim, S.-J., Crowley, T. J., Erickson, D. J., Govindasamy, B., Duffy, P. B. and Lee, B. Y.:
923 High-resolution climate simulation of the last glacial maximum, Clim Dynam, 31(1),
924 1–16, doi:10.1007/s00382-007-0332-z, 2007.

925 Köhl, A. and Stammer, D.: Decadal sea level changes in the 50-year GECCO ocean
926 synthesis, J Climate, 21(9), 1876–1890, doi:10.1175/2007JCLI2081.1, 2008.

927 Köhler, P., Bintanja, R., Fischer, H., Joos, F., Knutti, R., Lohmann, G. and Masson-
928 Delmotte, V.: What caused Earth's temperature variations during the last 800,000
929 years? Data-based evidence on radiative forcing and constraints on climate
930 sensitivity, Quaternary Sci Rev, 29(1–2), 129–145,
931 doi:10.1016/j.quascirev.2009.09.026, 2010.

932 Kump, L. R. and Pollard, D.: Amplification of cretaceous warmth by biological cloud
933 feedbacks, Science, 320(5873), 195–195, doi:10.1126/science.1153883, 2008.

934 Kutzbach, J. E. and Liu, Z.: Response of the African Monsoon to Orbital Forcing and
935 Ocean Feedbacks in the Middle Holocene, Science, 278(5337), 440–443,
936 doi:10.1126/science.278.5337.440, 1997.

937 Kutzbach, J. E. and Otto-Bliesner, B. L.: The Sensitivity of the African-Asian Monsoonal
938 Climate to Orbital Parameter Changes for 9000 Years Bp in a Low-Resolution

939 General-Circulation Model, Journal of the Atmospheric Sciences, 39(6), 1177–1188,
940 1982.

941 Kutzbach, J. E., Bartlein, P. J., FOLEY, J. A., Harrison, S. P., Hostetler, S. W., Liu, Z.,
942 Prentice, I. C. and WEBB, T. I.: Potential role of vegetation feedback in the climate
943 sensitivity of high-latitude regions : A case study at 6000 years B.P, Global
944 Biogeochem Cy, 10(4), 727–736, 1996a.

945 Kutzbach, J., Bonan, G., Foley, J. and Harrison, S. P.: Vegetation and soil feedbacks on
946 the response of the African monsoon to orbital forcing in the early to middle
947 Holocene, Nature, 384(6610), 623–626, doi:10.1038/384623a0, 1996b.

948 Kutzbach, J., Gallimore, R., Harrison, S., Behling, P., Selin, R. and Laarif, F.: Climate
949 and biome simulations for the past 21,000 years, Quaternary Sci Rev, 17(6-7), 473–
950 506, 1998.

951 Leduc, G., Schneider, R., Kim, J. H. and Lohmann, G.: Holocene and Eemian sea surface
952 temperature trends as revealed by alkenone and Mg/Ca paleothermometry,
953 Quaternary Sci Rev, 29(7-8), 989–1004, doi:10.1016/j.quascirev.2010.01.004, 2010.

954 Lee, J.-Y. and Wang, B.: Future change of global monsoon in the CMIP5, Clim Dynam,
955 42(1-2), 101–119, doi:10.1007/s00382-012-1564-0, 2014.

956 Li, C. and Battisti, D. S.: Reduced Atlantic Storminess during Last Glacial Maximum:
957 Evidence from a Coupled Climate Model, J Climate, 21(14), 3561–3579,
958 doi:10.1175/2007jcli2166.1, 2008.

959 Licciardi, J. M., Clark, P. U., Jenson, J. W. and Macayeal, D. R.: Deglaciation of a soft-
960 bedded Laurentide Ice Sheet, Quaternary Sci Rev, 17(4-5), 427–448,
961 doi:10.1016/S0277-3791(97)00044-9, 1998.

962 Lippold, J., Grützner, J., Winter, D., Lahaye, Y., Mangini, A. and Christl, M.: Does
963 sedimentary 231Pa/230Th from the Bermuda Rise monitor past Atlantic Meridional
964 Overturning Circulation? Geophys. Res. Lett., 36(12), L12601,
965 doi:10.1029/2009gl038068, 2009.

966 Liu, Z., Otto-Bliesner, B. L., He, F., Brady, E. C., Tomas, R., Clark, P. U., Carlson, A. E.,
967 Lynch-Stieglitz, J., Curry, W., Brook, E., Erickson, D., Jacob, R., Kutzbach, J. and
968 Cheng, J.: Transient Simulation of Last Deglaciation with a New Mechanism for
969 Bolling-Allerod Warming, Science, 325(5938), 310–314,
970 doi:10.1126/science.1171041, 2009.

971 Liu, Z., Zhu, J., Rosenthal, Y., Zhang, X., Otto-Bliesner, B. L., Timmermann, A., Smith,
972 R. S., Lohmann, G., Zheng, W. and Elison Timm, O.: The Holocene temperature
973 conundrum, Proceedings of the National Academy of Sciences,
974 doi:10.1073/pnas.1407229111, 2014.

975 Lynch-Stieglitz, J., Adkins, J. F., Curry, W. B., Dokken, T., Hall, I. R., Herguera, J. C.,
976 Hirschi, J. J., Ivanova, E. V., Kissel, C., Marchal, O., Marchitto, T. M., McCave, I.
977 N., McManus, J. F., Mulitza, S., Ninnemann, U., Peeters, F., Yu, E. F. and Zahn, R.:
978 Atlantic meridional overturning circulation during the Last Glacial Maximum,
979 Science, 316(5821), 66–69, doi:10.1126/science.1137127, 2007.

980 Marcott, S. A., Shakun, J. D., Clark, P. U. and Mix, A. C.: A Reconstruction of Regional
981 and Global Temperature for the Past 11,300 Years, Science, 339(6124), 1198–1201,
982 doi:10.1126/Science.1228026, 2013.

983 Marzin, C. and Braconnot, P.: Variations of Indian and African monsoons induced by
984 insolation changes at 6 and 9.5 kyr BP, Clim Dynam, 33(2-3), 215–231,
985 doi:10.1007/s00382-009-0538-3, 2009.

986 McManus, J. F., Francois, R., Gherardi, J. M., Keigwin, L. D. and Brown-Leger, S.:
987 Collapse and rapid resumption of Atlantic meridional circulation linked to deglacial
988 climate changes, Nature, 428(6985), 834–837, doi:10.1038/Nature02494, 2004.

989 Meehl, G. A., Stocker, T. F. and Collins, W. D.: Global climate projections, in Climate
990 Change 2007: The Physical Science Basis. Contribution of Working Group I to the
991 Fourth Assessment Report of the Intergovernmental Panel on Climate Change, edited
992 by S. Solomon, D. Qin, M. Manning, Z. Chen, M. Marquis, K. B. Averyt, M. Tignor,
993 and H. L. Miller, Cambridge University Press, Cambridge, United Kingdom and New
994 York, NY, USA. 2007.

995 Miller, G., Mangan, J., Pollard, D., Thompson, S. L., Felzer, B. and Magee, J.: Sensitivity
996 of the Australian Monsoon to insolation and vegetation: Implications for human
997 impact on continental moisture balance, Geology, 33(1), 65–68, 2005.

998 Moller, T., Schulz, H. and Kucera, M.: The effect of sea surface properties on shell
999 morphology and size of the planktonic foraminifer Neogloboquadrina pachyderma in
1000 the North Atlantic, Palaeogeography, Palaeoclimatology, Palaeoecology, 391, 34–48,
1001 doi:10.1016/j.palaeo.2011.08.014, 2013.

1002 Monnin, E., Indermuhle, A., Dallenbach, A., Fluckiger, J., Stauffer, B., Stocker, T. F.,
1003 Raynaud, D. and Barnola, J. M.: Atmospheric CO2 concentrations over the last
1004 glacial termination, Science, 291(5501), 112–114, 2001.

1005 Otto-Bliesner, B. L., Brady, E. C., Clauzet, G., Tomas, R., Levis, S. and Kothavala, Z.:
1006 Last Glacial Maximum and Holocene climate in CCSM3, J Climate, 19(11), 2526–
1007 2544, doi:10.1175/Jcli3748.1, 2006a.

1008 Otto-Bliesner, B. L., Schneider, R., Brady, E. C., Kucera, M., Abe-Ouchi, A., Bard, E.,
1009 Braconnot, P., Crucifix, M., Hewitt, C. D., Kageyama, M., Marti, O., Paul, A.,
1010 Rosell-Mele, A., Waelbroeck, C., Weber, S. L., Weinelt, M. and Yu, Y.: A
1011 comparison of PMIP2 model simulations and the MARGO proxy reconstruction for
1012 tropical sea surface temperatures at last glacial maximum, Clim Dynam, 32(6), 799–
1013 815, doi:10.1007/s00382-008-0509-0, 2009.

1014 Otto-Bliesner, B. L., Tomas, R., Brady, E. C., Ammann, C., Kothavala, Z. and Clauzet,
1015 G.: Climate sensitivity of moderate- and low-resolution versions of CCSM3 to
1016 preindustrial forcings, J Climate, 19(11), 2567–2583, doi:10.1175/Jcli3754.1, 2006b.

1017 Pacanowski, R. C.: MOM 2 Version 2.0 (Beta) Documentation: User's Guide and
1018 Reference Manual, NOAA GFDL Ocean Technical Report 3.2. 1996.

1019 Pausata, F. S. R., Li, C., Wettstein, J. J., Kageyama, M. and Nisancioglu, K. H.: The key
1020 role of topography in altering North Atlantic atmospheric circulation during the last
1021 glacial period, Clim Past, 7(4), 1089–1101, doi:10.5194/cp-7-1089-2011, 2011.

1022 Peixoto, J. P. and Oort, A. H.: Physics of climate, American Institute of Physics, New
1023 York. 1992.

1024 Peltier, W. R.: Global glacial isostatic adjustment: palaeogeodetic and space-geodetic
1025 tests of the ICE-4G (VM2) model, Journal of Quaternary Science, 17(5-6), 491–510,
1026 doi:10.1002/jqs.713, 2002.

1027 Pinot, S., Ramstein, G., Harrison, S. P., Prentice, I. C., Guiot, J., Stute, M. and
1028 Joussaume, S.: Tropical paleoclimates at the Last Glacial Maximum: comparison of
1029 Paleoclimate Modeling Intercomparison Project (PMIP) simulations and paleodata,
1030 Clim Dynam, 15(11), 857–874, 1999.

1031 Pollard, D. and Reusch, D. B.: A calendar conversion method for monthly mean
1032 paleoclimate model output with orbital forcing, J.-Geophys.-Res., 107(D22), 4615,
1033 doi:10.1029/2002JD002126, 2002.

1034 Pollard, D. and Thompson, S. L.: Sea‐ice dynamics and CO 2sensitivity in a global
1035 climate model, Atmosphere-Ocean, 32(2), 449–467,
1036 doi:10.1080/07055900.1994.9649506, 1994.

1037 Pollard, D. and Thompson, S. L.: Use of a Land-Surface-Transfer Scheme (Lsx) in a
1038 Global Climate Model - the Response to Doubling Stomatal-Resistance, Global
1039 Planet Change, 10(1-4), 129–161, doi:10.1016/0921-8181(94)00023-7, 1995.

1040 Pollard, D. and Thompson, S. L.: Climate and ice-sheet mass balance at the last glacial
1041 maximum from the genesis version 2 global climate model, Quaternary Sci Rev,
1042 16(8), 841–863, 1997.

1043 Pollard, D., Bergengren, J. C., Stillwell-Soller, L. M., Felzer, B. and Thompson, S. L.:
1044 Climate simulations for 10000 and 6000 years BP using the GENESIS global climate
1045 model. Palaeoclimates: Data and Modelling, Palaeoclimates - Data and Modelling.
1046 1998.

1047 Poulsen, C. J., Pollard, D. and White, T. S.: General circulation model simulation of the
1048 delta O-18 content of continental precipitation in the middle Cretaceous: A model-
1049 proxy comparison, Geology, 35(3), 199–202, doi:10.1130/G23343A.1, 2007a.

1050 Poulsen, C. J., Pollard, D., Montanez, I. P. and Rowley, D.: Late Paleozoic tropical
1051 climate response to Gondwanan deglaciation, Geology, 35(9), 771–774,
1052 doi:10.1130/G23841A.1, 2007b.

1053 Ramstein, G. and Joussaume, S.: Sensitivity experiments to sea surface temperatures, sea-
1054 ice extent and ice-sheet reconstruction for the Last Glacial Maximum, Annals of
1055 Glaciology, 21, 343–347, 1995.

1056 Renssen, H., Goosse, H., Fichefet, T., Brovkin, V., Driesschaert, E. and Wolk, F.:
1057 Simulating the Holocene climate evolution at northern high latitudes using a coupled
1058 atmosphere-sea ice-ocean-vegetation model, Clim Dynam, 24(1), 23–43,
1059 doi:10.1007/s00382-004-0485-y, 2004.

1060 Rind, D.: Components of the Ice-Age Circulation, J.-Geophys.-Res., 92(D4), 4241–4281,
1061 1987.

1062 Roche, D. M., Crosta, X. and Renssen, H.: Evaluating Southern Ocean sea-ice for the
1063 Last Glacial Maximum and pre-industrial climates: PMIP-2 models and data
1064 evidence, Quaternary Sci Rev, 56, 99–106, doi:10.1016/j.quascirev.2012.09.020,
1065 2012.

1066 Roche, D. M., Dokken, T. M., Goosse, H., Renssen, H. and Weber, S. L.: Climate of the
1067 Last Glacial Maximum: sensitivity studies and model-data comparison with the
1068 LOVECLIM coupled model, Clim Past, 3(2), 205–224, 2007.

1069 Rohling, E. J., Medina-Elizalde, M., Shepherd, J. G., Siddall, M. and Stanford, J. D.: Sea
1070 Surface and High-Latitude Temperature Sensitivity to Radiative Forcing of Climate
1071 over Several Glacial Cycles, J. Climate, 25(5), 1635–1656,
1072 doi:10.1175/2011JCLI4078.1, 2012.

1073 Ruddiman, W. F., Vavrus, S. J. and Kutzbach, J. E.: A test of the overdue-glaciation
1074 hypothesis, Quaternary Sci Rev, 24(1-2), 1–10, doi:10.1016/j.quascirev.2004.07.010,
1075 2005.

1076 Russell, J. L., Stouffer, R. J. and Dixon, K. W.: Intercomparison of the Southern Ocean
1077 circulations in IPCC coupled model control simulations, J Climate, 19(18), 4560–
1078 4575, doi:10.1175/Jcli3869.1, 2006.

1079 Schmittner, A., Latif, M. and Schneider, B.: Model projections of the North Atlantic
1080 thermohaline circulation for the 21st century assessed by observations, Geophys. Res.
1081 Lett., 32(23), L23710, doi:10.1029/2005gl024368, 2005.

1082 Schmittner, A., Silva, T. A. M., Fraedrich, K., Kirk, E. and Lunkeit, F.: Effects of
1083 Mountains and Ice Sheets on Global Ocean Circulation, J Climate, 24(11), 2814–
1084 2829, doi:10.1175/2010jcli3982.1, 2011a.

1085 Schmittner, A., Urban, N. M., Shakun, J. D., Mahowald, N. M., Clark, P. U., Bartlein, P.
1086 J., Mix, A. C. and Rosell-Mele, A.: Climate sensitivity estimated from temperature

1087 reconstructions of the Last Glacial Maximum, Science, 334(6061), 1385–1388,
1088 doi:10.1126/science.1203513, 2011b.

1089 Semtner, A. J.: A Model for the Thermodynamic Growth of Sea Ice in Numerical
1090 Investigations of Climate, J. Phys. Oceanogr., 6(3), 379–389, doi:10.1175/1520-
1091 0485(1976)006<0379:AMFTTG>2.0.CO;2, 1976.

1092 Shakun, J. D., Clark, P. U., He, F., Marcott, S. A., Mix, A. C., Liu, Z., Otto-Bliesner, B.
1093 L., Schmittner, A. and Bard, E.: Global warming preceded by increasing carbon
1094 dioxide concentrations during the last deglaciation, Nature, 484(7392), 49–54,
1095 doi:10.1038/nature10915, 2012.

1096 Singarayer, J. S. and Valdes, P. J.: High-latitude climate sensitivity to ice-sheet forcing
1097 over the last 120 kyr, Quaternary Sci Rev, 29(1-2), 43–55,
1098 doi:10.1016/j.quascirev.2009.10.011, 2010.

1099 Smith, R. S. and Gregory, J.: The last glacial cycle: transient simulations with an
1100 AOGCM, Clim Dynam, 38(7-8), 1545–1559, doi:10.1007/s00382-011-1283-y, 2012.

1101 Sowers, T., Alley, R. B. and Jubenville, J.: Ice core records of atmospheric N2O covering
1102 the last 106,000 years, Science, 301(5635), 945–948, 2003.

1103 Srokosz, M., Baringer, M., Bryden, H., Cunningham, S., Delworth, T., Lozier, S.,
1104 Marotzke, J. and Sutton, R.: Past, Present, and Future Changes in the Atlantic
1105 Meridional Overturning Circulation, Bull. Amer. Meteor. Soc., 93(11), 1663–1676,
1106 doi:10.1175/bams-d-11-00151.1, 2012.

1107 Tabor, C. R., Poulsen, C. J. and Pollard, D.: Mending Milankovitch's theory: obliquity
1108 amplification by surface feedbacks, Clim Past, 10(1), 41–50, doi:10.5194/cp-10-41-
1109 2014, 2014.

1110 Thompson, S. L. and Pollard, D.: A Global Climate Model (Genesis) with a Land-Surface
1111 Transfer Scheme (Lsx) .1. Present Climate Simulation, J Climate, 8(4), 732–761,
1112 1995.

1113 Thompson, S. L. and Pollard, D.: Greenland and Antarctic mass balances for present and
1114 doubled atmospheric CO2 from the GENESIS version-2 global climate model, J
1115 Climate, 10(5), 871–900, 1997.

1116 Timm, O. and Timmermann, A.: Simulation of the Last 21 000 Years Using Accelerated
1117 Transient Boundary Conditions, J Climate, 20(17), 4377–4401,
1118 doi:10.1175/JCLI4237.1, 2007.

1119 Timm, O., Köhler, P., Timmermann, A. and Menviel, L.: Mechanisms for the onset of the
1120 African humid period and Sahara greening 14.5–11 ka BP, J Climate, 23(10), 2612–
1121 2633, doi:10.1175/2010jcli3217.1, 2010.

1122 Timm, O., Timmermann, A., Abe-Ouchi, A., Saito, F. and Segawa, T.: On the definition
1123 of seasons in paleoclimate simulations with orbital forcing, Paleoceanography, 23(2),
1124 PA2221, doi:10.1029/2007PA001461, 2008.

1125 Ullman, D. J., LeGrande, A. N., Carlson, A. E., Anslow, F. S. and Licciardi, J. M.:
1126 Assessing the impact of Laurentide Ice Sheet topography on glacial climate, Clim
1127 Past, 10(2), 487–507, doi:10.5194/cp-10-487-2014, 2014.

1128 Unterman, M. B., Crowley, T. J., Hodges, K. I., Kim, S. J. and Erickson, D. J.:
1129 Paleometeorology: High resolution Northern Hemisphere wintertime mid-latitude
1130 dynamics during the Last Glacial Maximum, Geophys. Res. Lett., 38(23), L23702,
1131 doi:10.1029/2011gl049599, 2011.

1132 Waelbroeck, C., Paul, A., Kucera, M., Rosell-Mele, A., Weinelt, M., Schneider, R., Mix,
1133 A. C., Abelmann, A., Armand, L., Bard, E., Barker, S., Barrows, T. T., Benway, H.,
1134 Cacho, I., Chen, M. T., Cortijo, E., Crosta, X., de Vernal, A., Dokken, T., Duprat, J.,
1135 Elderfield, H., Eynaud, F., Gersonde, R., Hayes, A., Henry, M., Hillaire-Marcel, C.,
1136 Huang, C. C., Jansen, E., Juggins, S., Kallel, N., Kiefer, T., Kienast, M., Labeyrie, L.,
1137 Leclaire, H., Londeix, L., Mangin, S., Matthiessen, J., Marret, F., Meland, M., Morey,
1138 A. E., Mulitza, S., Pflaumann, U., Pisias, N. G., Radi, T., Rochon, A., Rohling, E. J.,
1139 Sbaffi, L., Schaefer-Neth, C., Solignac, S., Spero, H., Tachikawa, K., Turon, J. L. and
1140 Members, M. P.: Constraints on the magnitude and patterns of ocean cooling at the
1141 Last Glacial Maximum, Nature Geoscience, 2(2), 127–132, doi:10.1038/NGEO411,
1142 2009.

1143 Weber, S. L., Drijfhout, S. S., Abe-Ouchi, A., Crucifix, M., Eby, M., Ganopolski, A.,
1144 Murakami, S., Otto-Bliesner, B. L. and Peltier, W. R.: The modern and glacial
1145 overturning circulation in the Atlantic Ocean in PMIP coupled model simulations,
1146 Clim Past, 3(1), 51–64, 2007.

1147 Zhao, Y. and Harrison, S. P.: Mid-Holocene monsoons: a multi-model analysis of the
1148 inter-hemispheric differences in the responses to orbital forcing and ocean feedbacks,
1149 Clim Dynam, 39(6), 1457–1487, doi:10.1007/s00382-011-1193-z, 2012.

1150 Zheng, W. and Braconnot, P.: Characterization of Model Spread in PMIP2 Mid-Holocene
1151 Simulations of the African Monsoon, J Climate, 26(4), 1192–1210,
1152 doi:10.1175/JCLI-D-12-00071.1, 2013.

1153 Zhou, J., Poulsen, C. J., Pollard, D. and White, T. S.: Simulation of modern and middle
1154 Cretaceous marine δ18O with an ocean-atmosphere general circulation model,
1155 Paleoceanography, 23(3), PA3223, doi:10.1029/2008pa001596, 2008.

1156

1157

Table 1. Atmospheric greenhouse gas concentrations for each time slice simulation. The 21 ka through 3 ka values for CO_2 (Monnin et al., 2001), CH_4 (Brook et al., 2000) and N_2O (Sowers et al., 2003) are estimated from ice core records by averaging the gas concentrations within a ± 300 yr window centered at the time of interest. For comparison, the PMIP3 concentrations for 6 ka are 280 ppmV, 650 ppbV, and 270 ppbV for CO_2, CH_4 and N_2O respectively, and 185 ppmV, 350 ppbV, and 200 ppbV for 21 ka. In the table, e is eccentricity, ω-180 is precession and ε is obliquity (Berger and Loutre, 1991).

	CO_2 (ppmV)	CH_4 (ppbV)	N_2O (ppbV)	e	ω-180	ε
PD	355	1714	311	0.0176	101.37	23.446
PI	280	760	270	0.0176	101.37	23.446
3 ka	275	627	264	0.0183	50.30	23.815
6 ka	260	596	227	0.0192	0.01	24.100
9 ka	260	677	244	0.0198	310.32	24.229
12 ka	240	500	246	0.0201	261.07	24.161
15 ka	220	500	216	0.0202	212.04	23.895
18 ka	188	382	219	0.0199	163.04	23.475
21 ka	188	392	199	0.0194	113.98	22.989

Table 2. Annual average 2-m air temperatures and precipitation rates for the time slice simulations. NCEP is from the National Center for Environmental Predication NCEP/NCAR Reanalysis data set (Kalnay et al., 1996), PD2X is the $2xCO_2$ simulation, PD is present day and PI is pre-industrial. Parenthetical values are the changes from the previous time slice, e.g., the global average temperature for the PD is 0.77 °C warmer than the PI.

	Temperature (K)			Precipitation (mm d^{-1})		
	Global	Land	Ocean	Global	Land	Ocean
NCEP (1980-2000)	287.52 --	281.66 --	289.84 --	3.09 --	2.30 --	3.40 --
PD2X	288.48 (2.2)	282.06 (2.69)	291.29 (1.91)	3.11 (0.11)	2.17 (0.10)	3.53 (0.13)
PD	286.34 (0.77)	279.37 (0.93)	289.38 (0.70)	3.00 (0.04)	2.07 (0.04)	3.40 (0.05)
PI	285.57 (0.07)	278.44 (-0.03)	288.68 (0.15)	2.95 (0.00)	2.03 (-0.02)	3.36 (0.02)
3 ka	285.50 (0.32)	278.47 (0.30)	288.53 (0.33)	2.95 (0.02)	2.05 (0.00)	3.34 (0.04)
6 ka	285.17 (0.23)	278.18 (0.95)	288.20 (-0.27)	2.93 (0.02)	2.05 (0.00)	3.30 (0.02)
9 ka	284.95 (0.74)	277.23 (1.63)	288.47 (0.22)	2.91 (0.05)	2.05 (0.06)	3.30 (0.03)
12 ka	284.21 (1.40)	275.60 (2.44)	288.25 (0.70)	2.86 (0.09)	1.99 (0.12)	3.26 (0.05)
15 ka	282.81 (0.93)	273.16 (1.53)	287.55 (0.53)	2.77 (0.05)	1.87 (0.09)	3.21 (0.02)
18 ka	281.88 (0.16)	271.63 (0.28)	287.02 (0.06)	2.72 (0.01)	1.78 (0.01)	3.19 (0.01)
21 ka	281.72	271.35	286.96	2.71	1.78	3.18

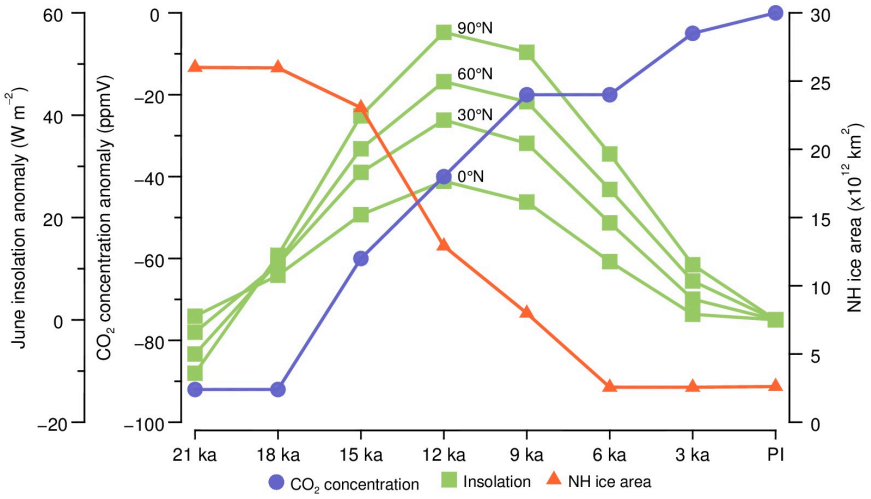

1177

1178 Fig. 1. Boundary conditions for the time slice simulations. CO_2 concentrations are

1179 relative to the PI concentration of 280 ppmV. NH ice area is the total area covered by the

1180 continental ice sheets. June insolation anomalies are relative to PI at the indicated

1181 latitude. Mid-month insolation data from Berger and Loutre (1991).

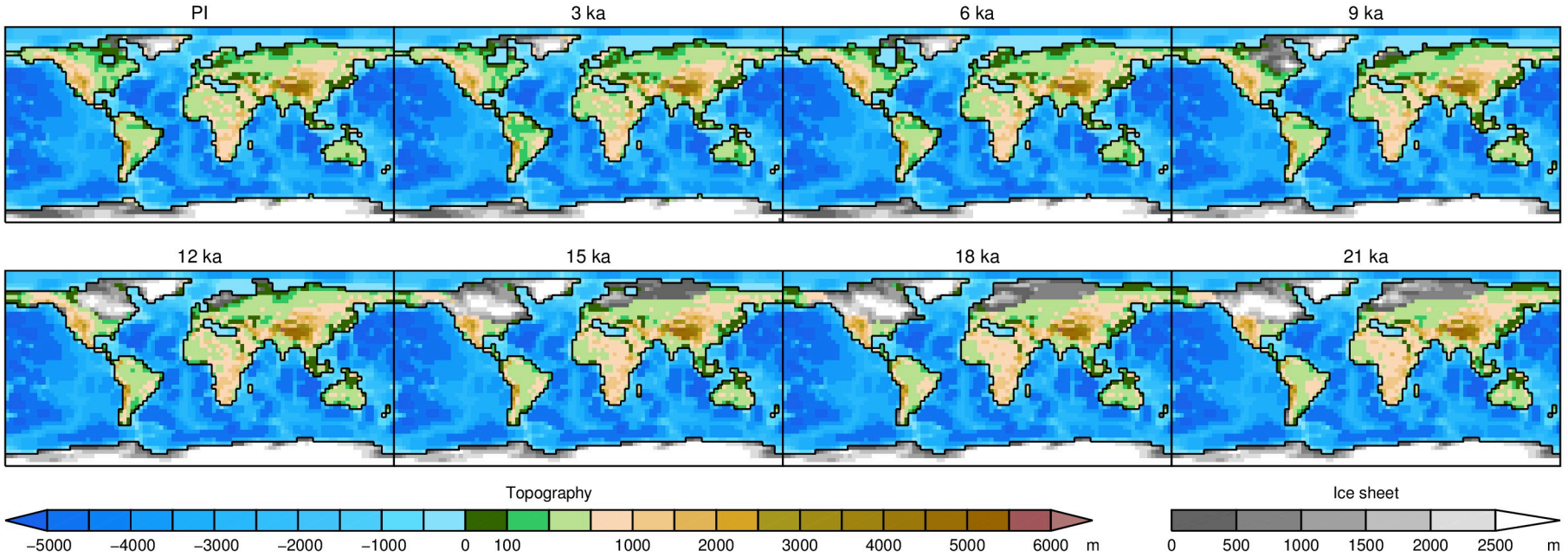

1182
1183 Fig. 2. Orography for the time slice simulations, with ice sheet height and extent derived from ICE-4G (Peltier, 2002) for the

1184 Fennoscandian, Cordilleran and Antarctic, and OSU-LIS (Licciardi et al., 1998) for the Laurentide.

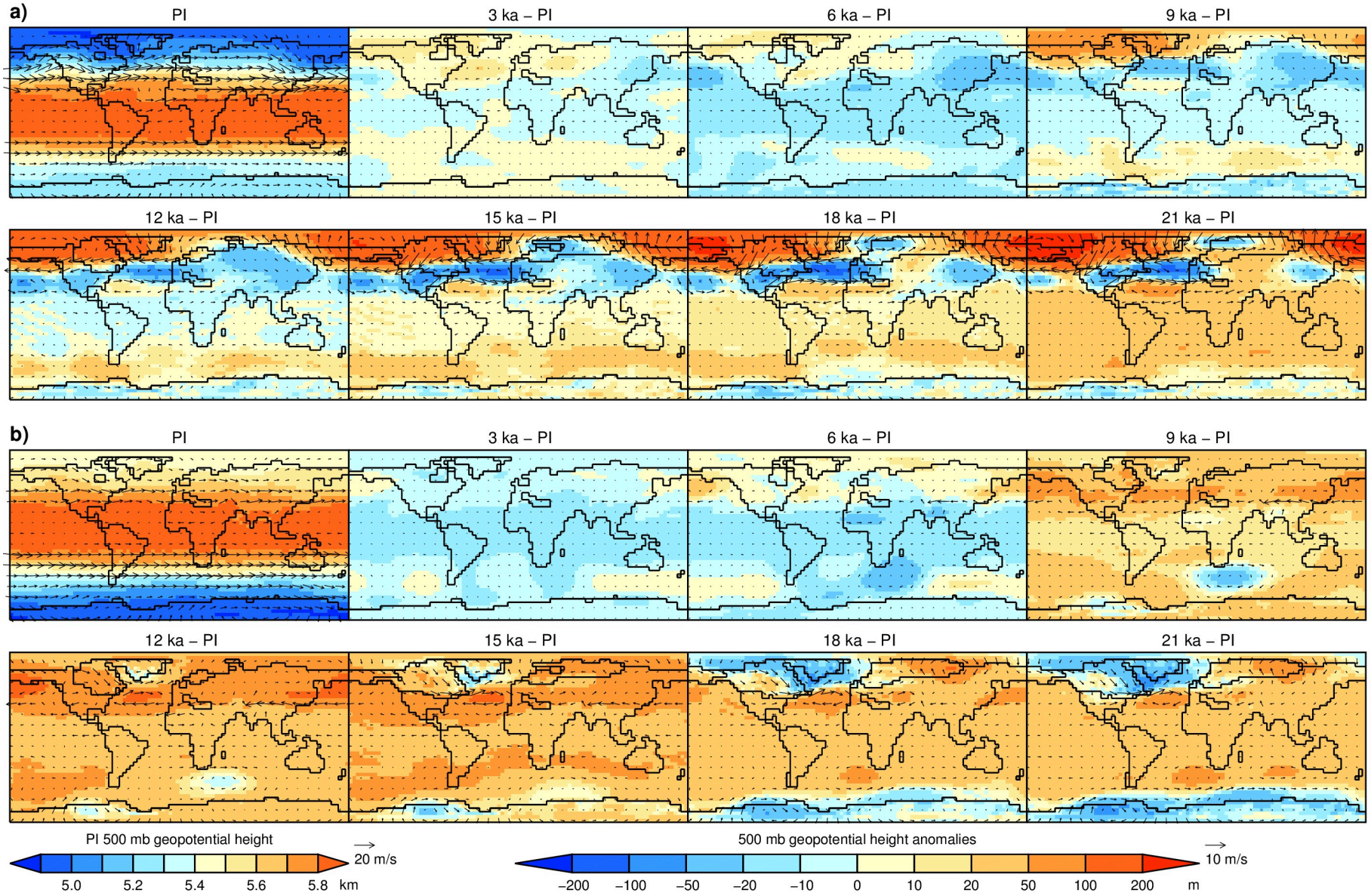

Fig. 3. Simulated seasonal 500 hPa geopotential height and wind anomalies relative to PI. a) December, January, and February and b) June, July and August. Raw 500 hPa geopotential height and wind are shown in SFig. 2.

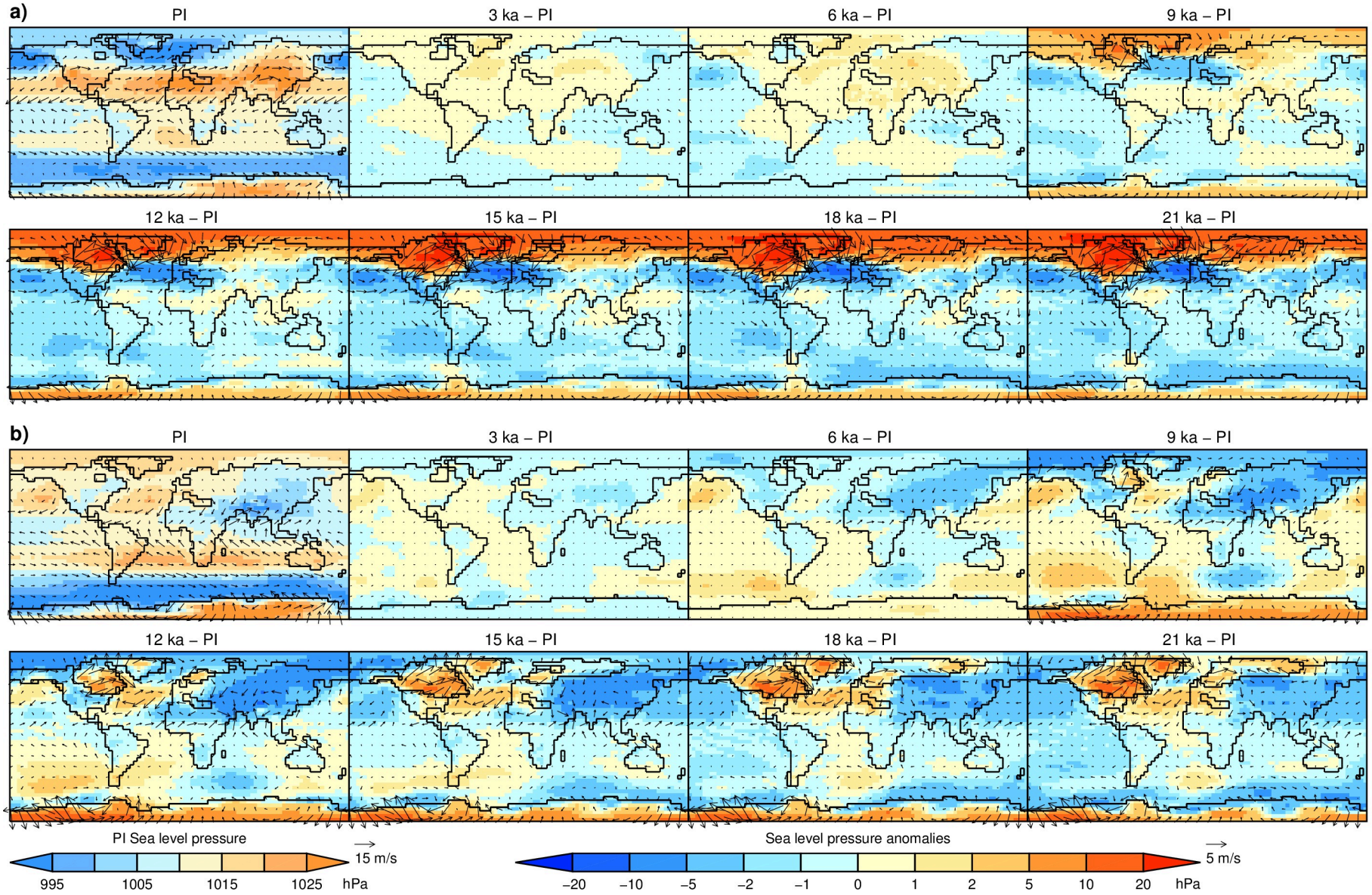

Fig. 4. Simulated seasonal average sea-level pressure and 2-m wind anomalies relative to PI. a) December, January, and February and b) June, July, and August. Raw sea level pressure and wind are shown in SFig. 3.

1191

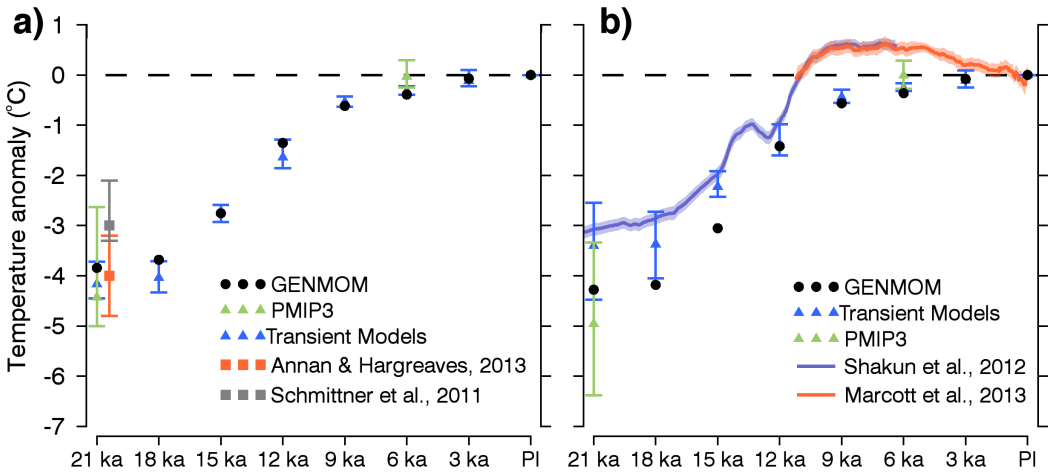

1192
1193

1194 Fig. 5. Simulated and reconstructed changes in temperature from 21 ka to present. a)
1195 Global mean surface air temperature from GENMOM compared to the PMIP3 ensemble
1196 average and three transient models (CCSM (Liu et al., 2009), LOVECLIM (Timm and
1197 Timmermann, 2007) and FAMOUS (Smith and Gregory, 2012)). The transient model
1198 values are averages over a ±50 yr window centered on the eight time slices. The symbols
1199 for the PMIP and transient models are the average of the ensembles and the bars
1200 represent the range of the ensembles. Data-model estimates of mean and range of LGM
1201 cooling by Annan and Hargreaves (2013) and Schmittner et al. (2011b) are offset from
1202 21 ka for legibility. b) Temperature change at the proxy sites used in the reconstructions
1203 by Shakun et al. (2012) and Marcott et al (2013). The models were bilinearly interpolated
1204 and aggregated to the 5° x 5° boxes around the proxy sites as in Marcott et al. (2013).

1205 The 1σ uncertainty in the reconstructions is indicated by the shaded band. Marcott et al.
1206 (2013) is adjusted to a pre-industrial (~1850) base value rather than the original 1961-
1207 1990. Data younger than pre-industrial are removed. The Shakun et al. (2012) and
1208 Marcott et al. (2013) time series are joined at their 11.5 ka – 6.5 ka means.

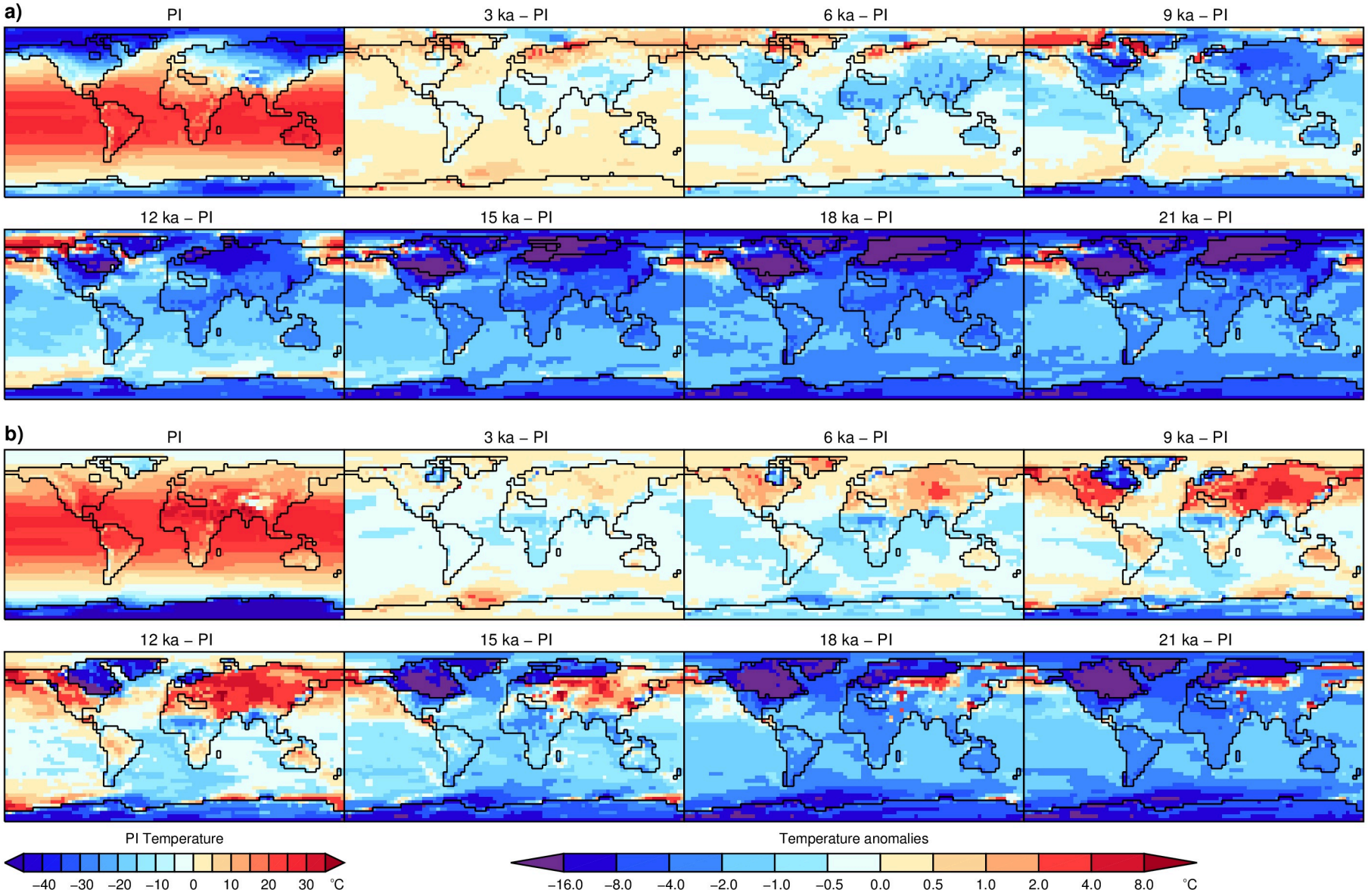

Fig. 6. Simulated seasonal average 2-m air temperature anomalies relative to PI. a) December, January, and February and b) June, July, and August.

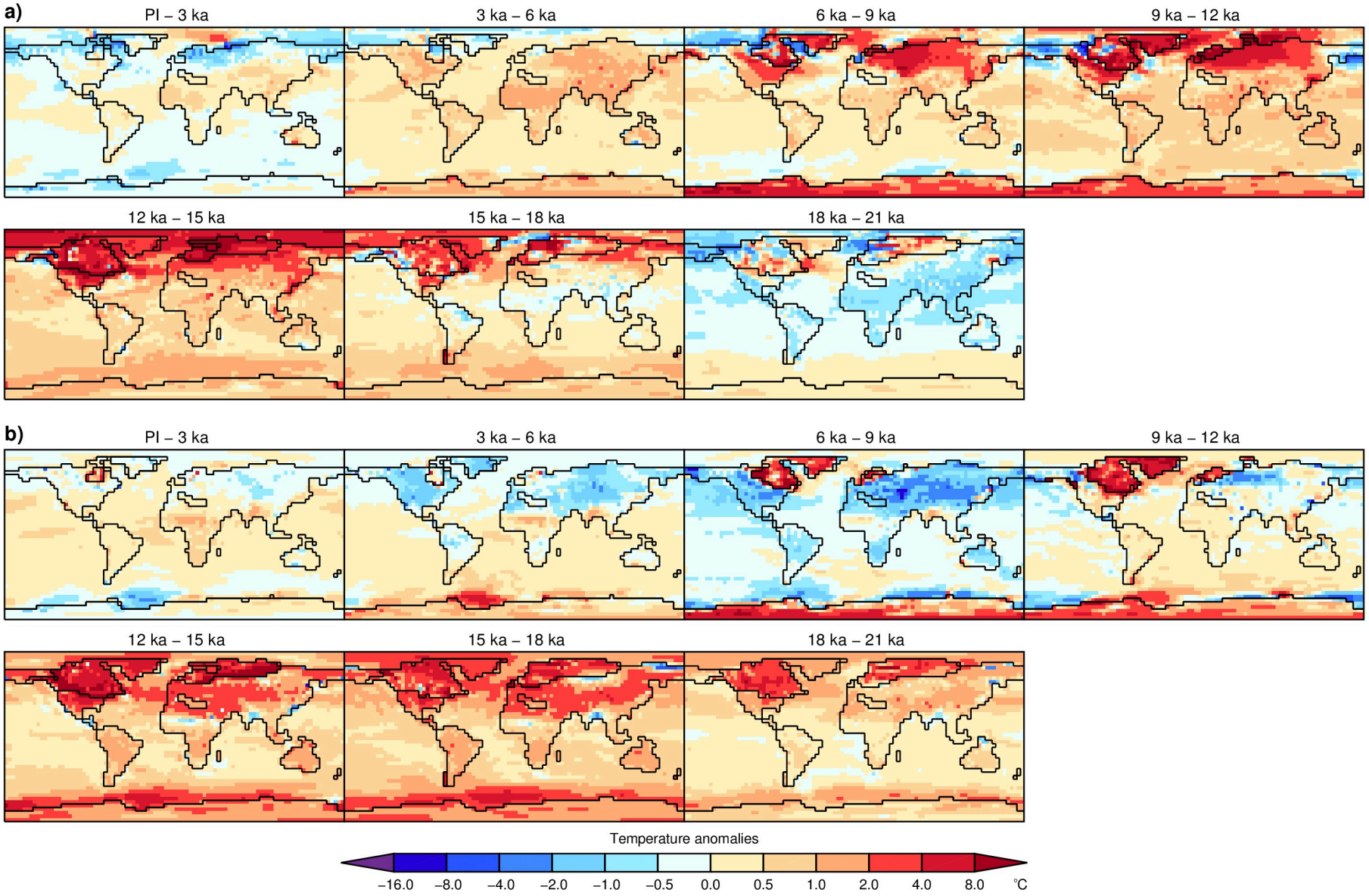

1212
1213 Fig. 7. Simulated seasonal average changes in 2-m air between consecutive time slices. a) December, January, and February and b)

1214 June, July, and August.

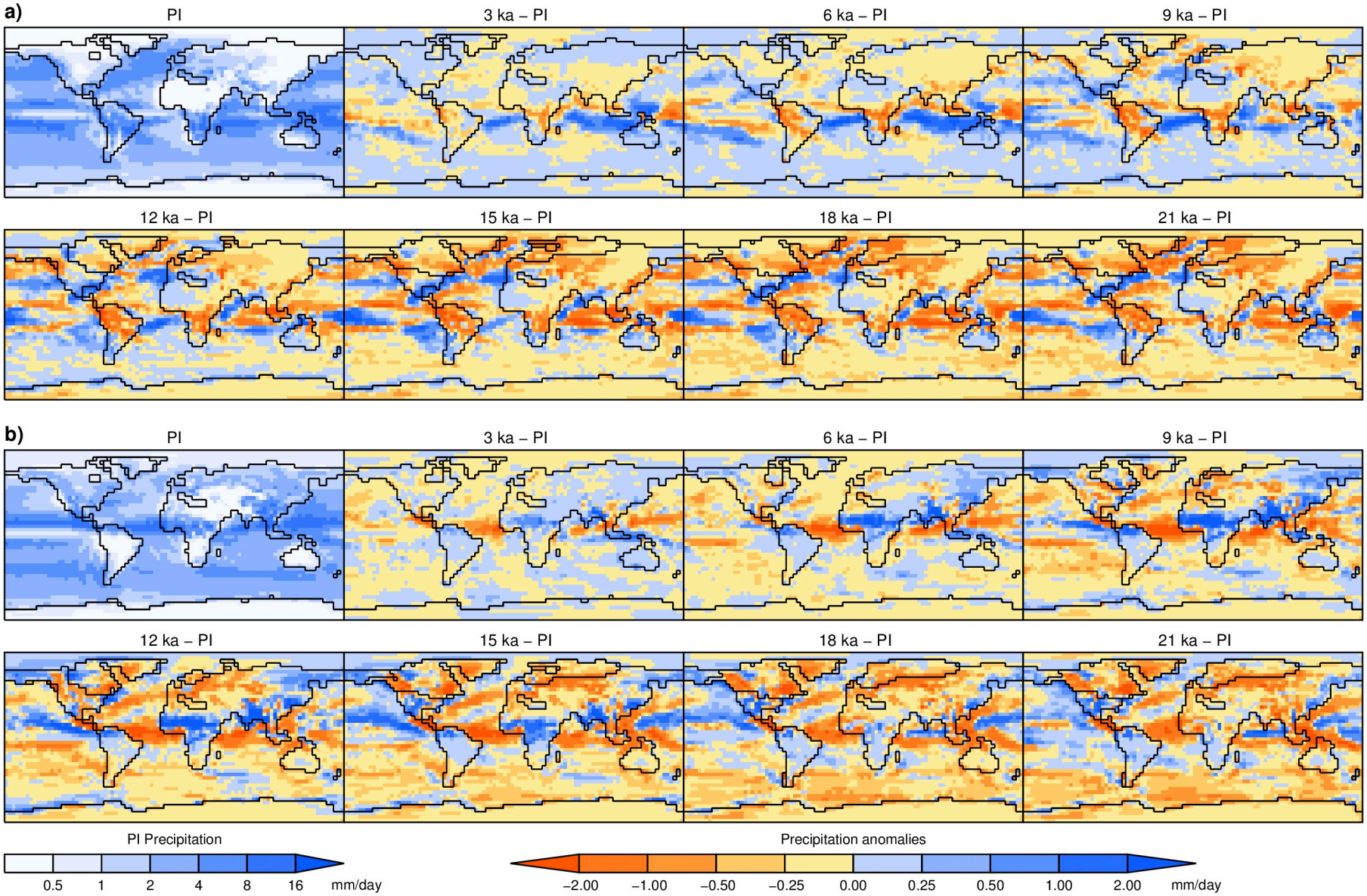

Fig. 8. Simulated seasonal average precipitation anomalies relative to PI. a) December, January, and February and b) June, July, and August.

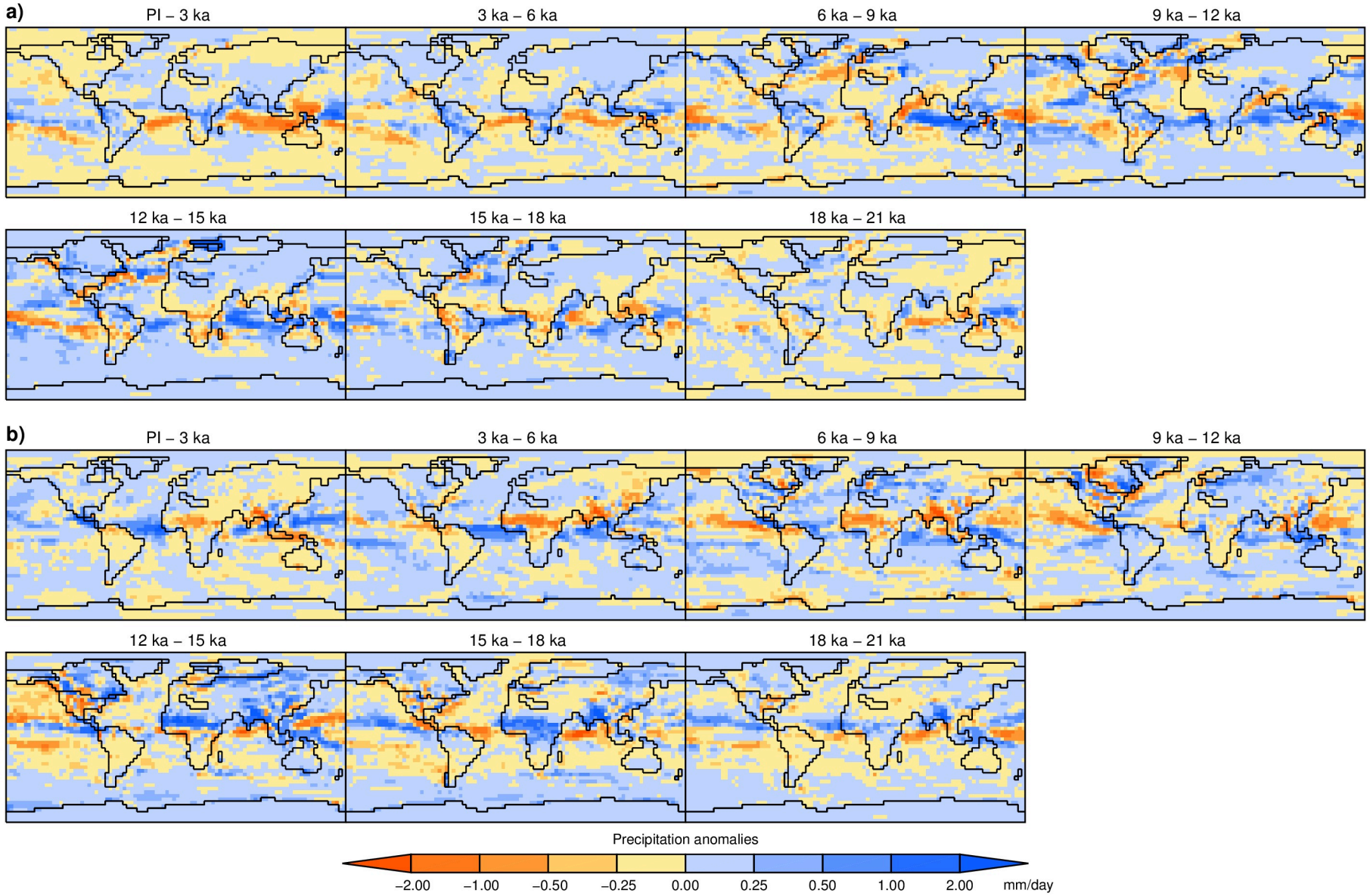

Fig. 9. Simulated seasonal average precipitation changes between consecutive time slices. a) December, January, and February and b) June, July, and August.

1221

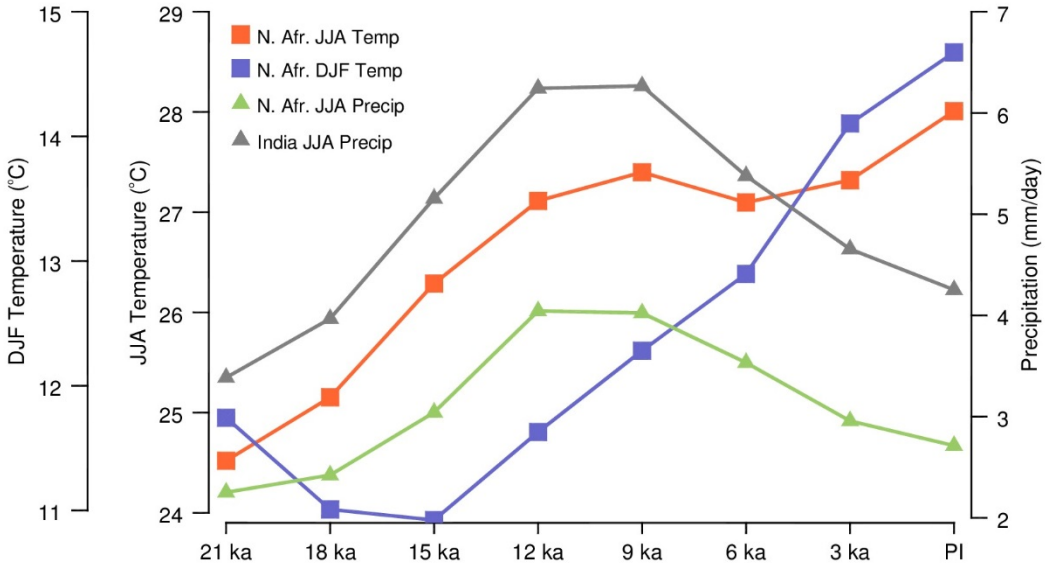

1222
1223

1224 Fig. 10. Time evolution of North African and Indian summer monsoons. The North

1225 Africa monsoon region is defined as 12°N - 30°N, 20°W - 30°E and India monsoon

1226 region is defined as 20°N - 40°N, 70°E - 100°E (Zhao and Harrison, 2012).

1227

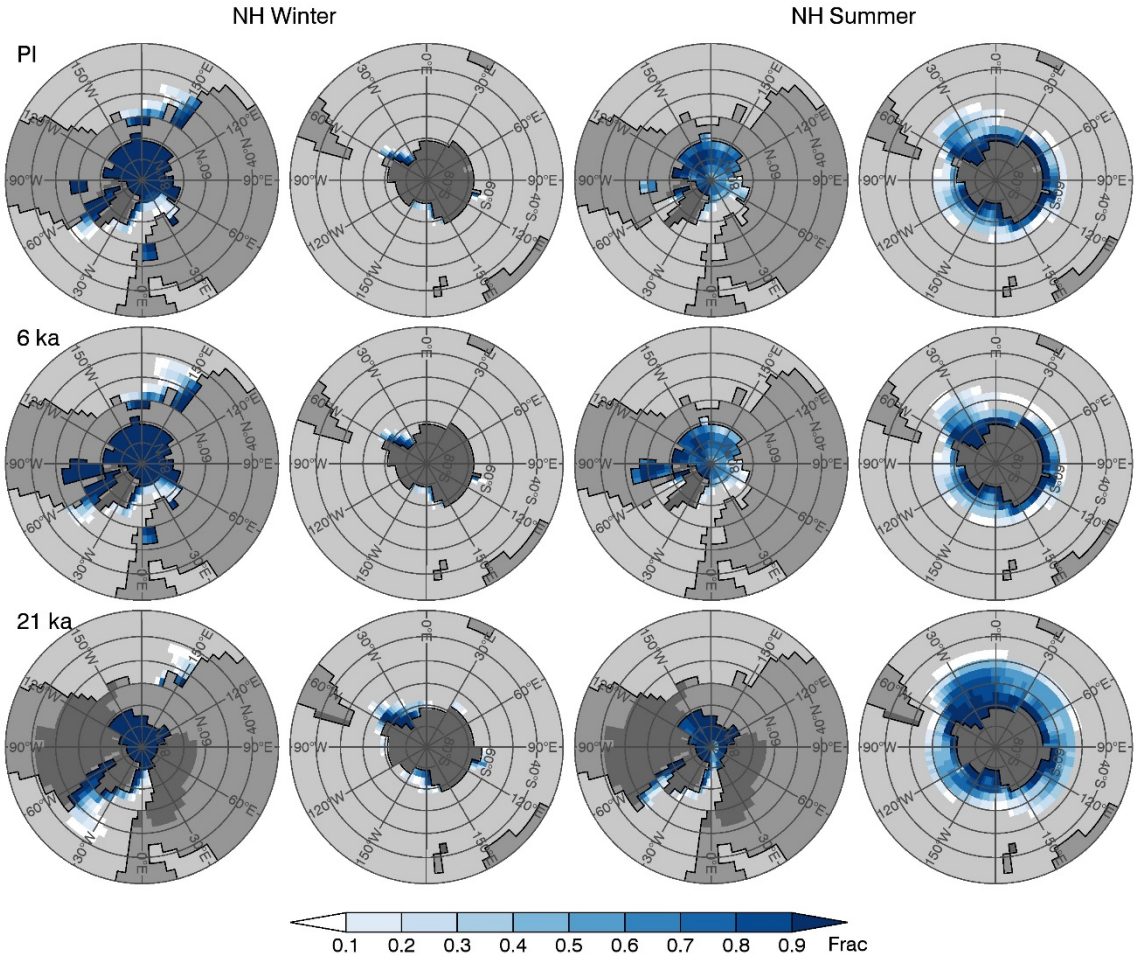

1227

1228 Fig. 11 Simulated sea-ice fraction for PI, 6 ka and 21 ka. Left two columns: February-

1229 March and right two columns: August-September. Medium gray is continental land mass

1230 and dark gray is continental ice sheet.

1231

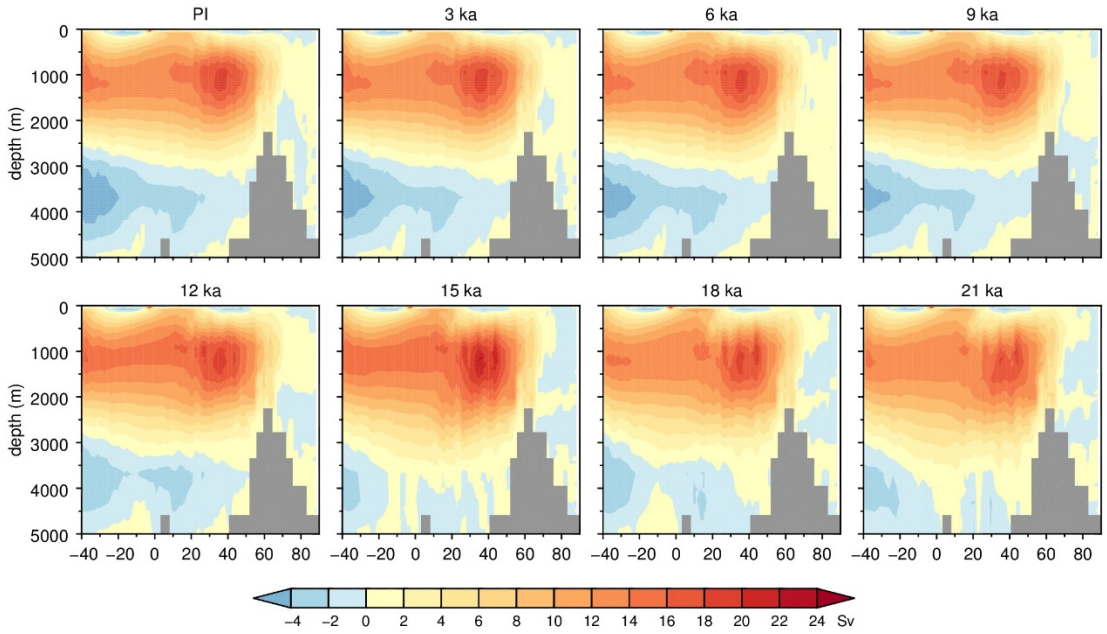

1231

1232 Fig. 12. Simulated annual average Atlantic Meridional Overturning Circulation (AMOC)

1233 for the eight time-slices.

1234

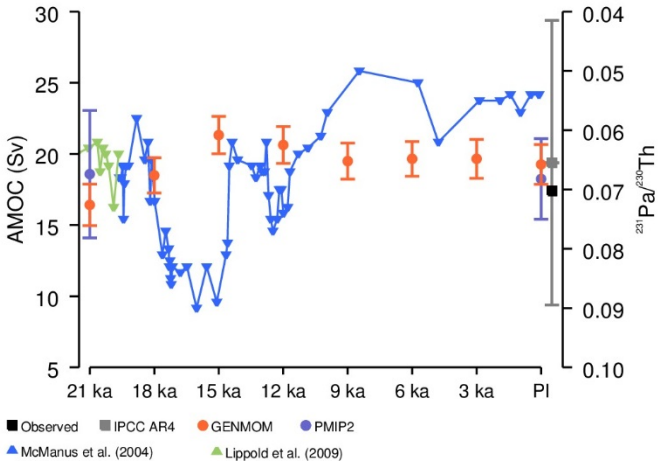

Fig. 13. Simulated Atlantic Meridional Overturning Circulation (AMOC) compared to $^{231}Pa/^{230}Th$ proxy record at 33°N and other AOGCMs. Observations are from 26.5°N. GENMOM values are 100-yr averages with error bars representing standard deviations. The mean and standard deviation of the maximum AMOC in the five PMIP2 models. The IPCC AR4 point represents the mean and standard deviation from a collection of IPCC AR4 models. $^{231}Pa/^{230}Th$ data from McManus et al. (2004) and Lippold et al. (2009); observed value from Srokosz et al. (2012), PMIP2 data from Weber et al. (2007), and IPCC data from Schmittner et al. (2005).

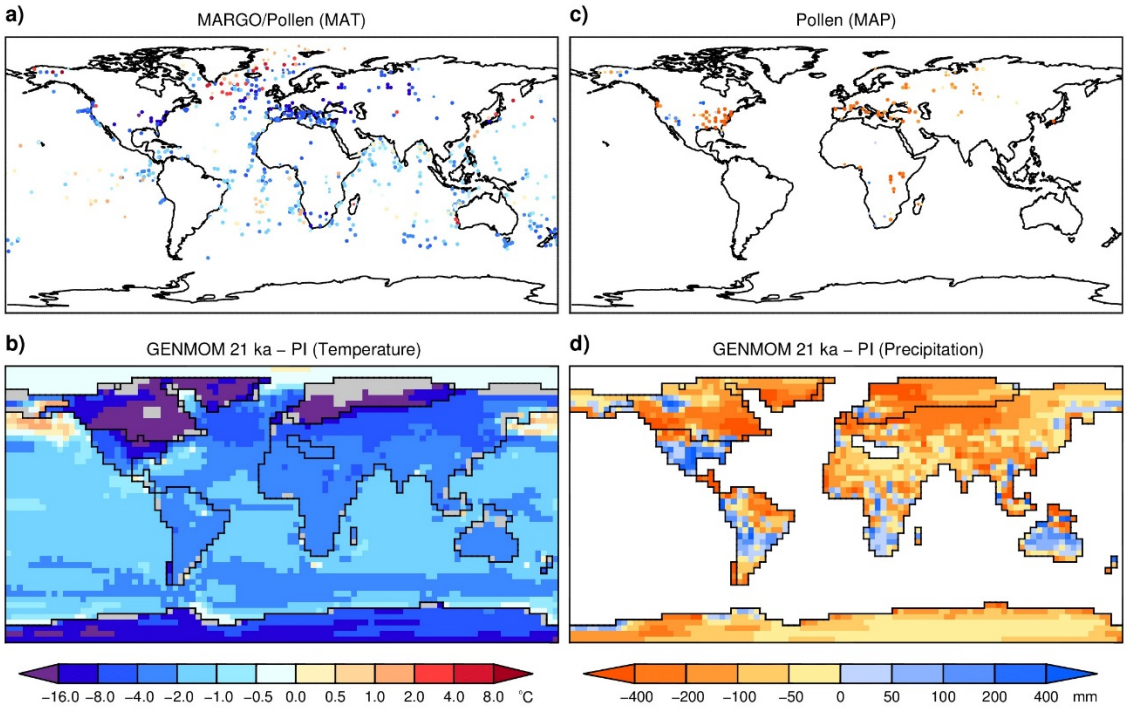

1243

1244 Fig. 14. Changes in 21 ka mean annual temperature (MAT) and precipitation (MAP)
1245 inferred from data and simulated by GENMOM. a) blended sea surface temperature from
1246 MARGO (Waelbroeck et al., 2009) and terrestrial temperature from Bartlein et al. (2011),
1247 b) GENMOM temperature anomalies (blended sea surface temperature and 2-m air
1248 temperature over land), c) precipitation from Bartlein et al. (2011), and d) GENMOM
1249 precipitation anomalies. Grid cells with different land mask types in the 21 ka and PI
1250 simulation are shaded in gray to avoid comparing ocean temperature to land temperature
1251 in emergent cells.

1252

1253

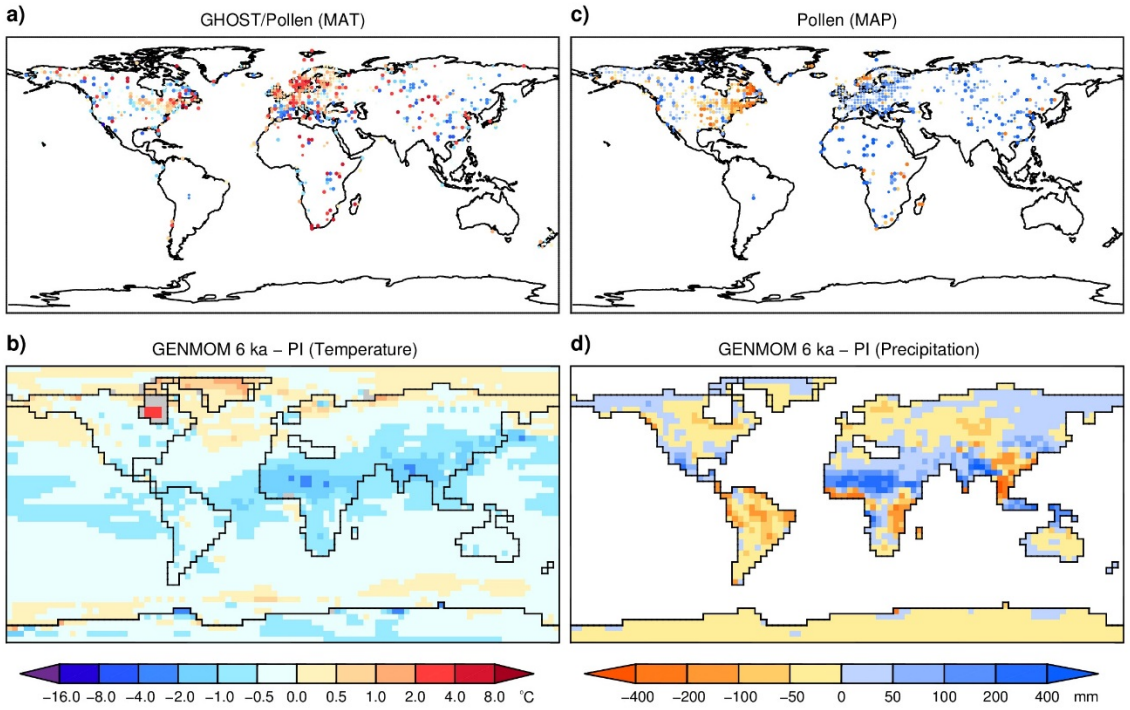

Fig. 15. Changes in 6 ka mean annual temperature (MAT) and precipitation (MAP) inferred from data and simulated by GENMOM. a) blended sea surface temperature from Leduc et al. (2010) and terrestrial temperature from Bartlein et al. (2011), b) GENMOM temperature anomalies (blended sea surface temperature and 2-m air temperature over land), c) precipitation from Bartlein et al. (2011) and d) GENMOM precipitation anomalies. Grid cells with different land mask types in the 6 ka and PI simulation are shaded in gray to avoid comparing ocean temperature to land temperature in emergent cells.